Raman spectroscopic investigation of radiation damage in carbon implanted diamond

A thesis submitted by

Linda C. Prinsloo

in fulfillment of the requirements for the degree of

Magister Scientiae
in
Chemistry

in the Faculty of Natural and Agricultural Sciences of the
University of Pretoria
Pretoria

Supervisor: Prof. E. Friedland

April 2001

ACKNOWLEDGEMENTS

I wish to express my sincere appreciation to the following people, who in one way or other, have contributed towards the completion of this study:

- Prof. E. Friedland, Department of Physics, University of Pretoria and Prof. S. Kalbitzer, Max-Planck-Institut für Kernphysik, Heidelberg, for including me in their research team.

- Prof. Friedland for his guidance and support throughout this study.

- Prof. Johan Brink, Department of Physics, University of Pretoria for his help in understanding the optics of the instruments I used.

- Prof. Anton Heyns, previously of the Chemistry Department, University of Pretoria, who introduced me to Raman and infrared spectroscopy and gave me the opportunity to attend courses abroad and gain exposure at international conferences.

- The Chemistry Department of the University of Pretoria for accepting me as an M.Sc. student.

- My husband Gerhard for editorial assistance and his continuous support.

RAMAN SPECTROSCOPIC INVESTIGATION OF RADIATION DAMAGE IN CARBON IMPLANTED DIAMOND

Candidate: Linda C Prinsloo

Supervisor: Prof. E Friedland

Degree: Magister Scientae in Chemistry

SUMMARY

Analog and digital structures can be written into thin surface layers of semiconductors by using focused ion beams of submicron dimensions. By inducing the phase transition from the crystalline (c) to the amorphous state (a) optical contrast is generated between areas of different exposure.

The aim of this study was to investigate the properties of diamond as a high-density optical recording medium and to determine the corresponding irradiation parameters. To this end, single crystals of diamond were irradiated with self-ions of 75 keV energy with fluences between F=0.3-10x10^{15} C/cm^2 at about 100 K.

The radiation damage, persisting after annealing treatments between 300-1700 K, was studied by Raman measurements, monitoring changes in the atomic bonding arrangements. Since the scattering cross-section of C sp^2 bonds is 50x that of C sp^3 bonds, this is an extremely sensitive technique in detecting changes in the initially purely sp^3 state. The position and linewidth of the characteristic first-order phonon of crystalline diamond at 1332 cm^{-1} reflect crystallinity and stress level, while bands between 1350-1700 cm^{-1} indicate disorder. In utilizing the microscopic resolution of a Raman facility additional information was obtained on the spatial variation of the damage level.

The optimum annealing temperature was found to be 1500 K. For F > 3x10^{15}C/cm^2, the damage was irreversible, for F = 3x10^{15}C/cm^2 the damage was only partly repaired after annealing at 1500 K and, for F < 3x10^{15}C/ cm^2, the crystalline/amorphous contrast was reversible. For F < 1x10^{15}C/ cm^2 Raman spectroscopy was not sensitive enough to

detect the incurred damage. Infrared spectroscopy was used to classify the diamond samples according to type.

CONTENTS

CHAPTER 1

INTRODUCTION

Worldwide, information technology has become one of the fastest growing industries, necessitating the digital storage of vast amounts of text, images and audio-visual materials fueled by multimedia requirements. Presently, much of this information is stored in magnetic archives, which are inherently unsafe with half-lives in the order of only 10 years under ambient temperature [1]. Alternative and improved methods that would offer higher data densities and prolonged stability are therefore needed to enhance the long-term preservation of invaluable electronically captured information.

One such promising alternative is optical recording, a method based on the modification of the optical properties of solids, such as semiconducters. So far, the optical storage of data does, however, not seem feasible by presently available optical techniques because of limitations with data density and storage lifetime [2, 3].

These limitations can, however, be overcome by using the novel ionographic technique. In modifying the optical properties of semiconducters such as silicon, silicon carbide and diamond, their amorphous state exhibits optical properties distinctly different from those of their crystalline state. At sub-band-gap photon energies the crystalline phase is practically transparent, while the amorphous phase strongly absorbs light. Focused beams of heavy ions can write patterns directly into the surface of the recording material by generating radiation damage to the exposed areas of semiconductors [4].

The above-mentioned principle of ionographic recording is illustrated in Fig. 1.1. Selected regions of a transparent crystalline material are exposed to a focused ion beam in order to render it opaque (amorphous). For readout incident light is fully transmitted through the non-irradiated parts of the film and fully absorbed in the irradiated region. In this way digital encoding of "0" and "1" can be achieved. Patterns formed in this way are practically infinitely stable at ambient temperatures and with beam spot sizes below 100nm, which can be

realized with modern ion beam equipment, analog or digital patterns can be written with densities of 10^{18}-10^{12}bit/cm^2. Compared to the $2x10^{10}$bit/cm^2 possible with magnetic hard disks this novel approach would mean enormous savings in terms of recording material and library storage space.

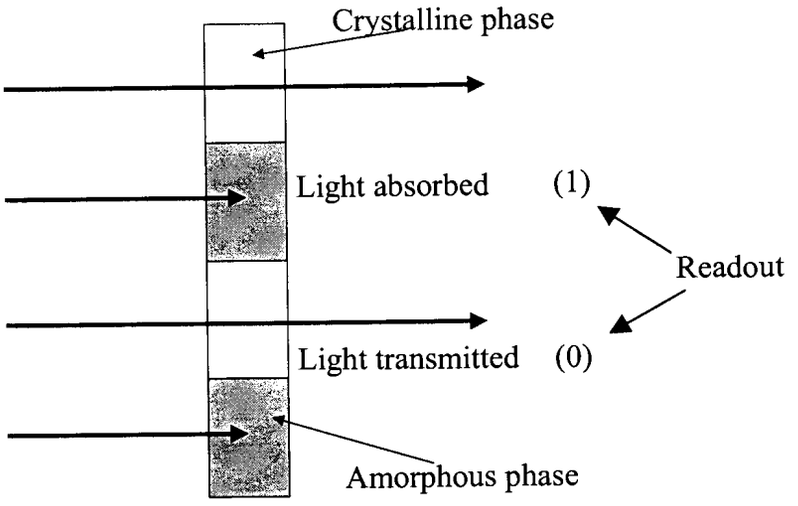

Figure 1.1: The principle of ionographic recording and readout.

Diamond, capable of transmitting light from the far-infrared to the ultraviolet, is the ideal optical material. Furthermore, the wide indirect band-gap of E_G=5,5eV shifts the useful range of light towards the violet region of the optical spectrum, thus improving the optical resolution limits accordingly. Given the other extreme properties of diamond, namely hardness and long-time stability, it would be the perfect material to use for permanent data storage.

Against this background a collaborative investigation within the Program of Scientific-Technical Cooperation between Germany and South Africa was launched during 1996 - 1999 to explore the feasibility of optical recording by irradiating diamond with energetic ion beams. The physical properties of the radiation effects were studied by a variety of techniques, including optical transmission and luminescence, photothermal deflection spectroscopy, infrared and Raman spectroscopy, and ion beam channeling in conjunction with atomic force measurements. The results of this study, which was conducted by a multidisciplinary team of

researchers from various institutions in South Africa and Germany, will appear as an invited contribution in *Applied Physics A,* **72**, 1-32 (2001) [5] and will include part of the work discussed in this thesis.

This thesis is based on an investigation pertaining to two of the above-mentioned techniques, namely infrared and Raman spectroscopy. These methods have been chosen because various studies have shown that they are important non-destructive characterization tools in the basic research of the physics and chemistry of carbon [6-14]. Both techniques are very sensitive to the nature of carbon bonding and can distinguish between various types of carbon, namely diamond, graphite, fullerenes, amorphous carbon and hydrogenated carbon. Information about the nature of the irradiated damage could therefore be obtained and by utilizing the microscopic resolution of a Raman microprobe additional information was obtained on the spatial variation of the damage level.

The chapters that follow deal with the theory behind the techniques, the vibrational spectra of carbon and its allotropes, a brief literature review of previous work on ion-implanted diamond samples, the instruments used, and experimental procedures. The results, conclusions and possible future work are also discussed.

CHAPTER 2

THEORETICAL BACKGROUND

2.1 Raman and infrared spectroscopy

Spectroscopy is the interpretation and prediction of the interaction of electromagnetic radiation with matter. In Fig.2.1 the electromagnetic spectrum is illustrated from low energy radio waves to high-energy γ-ray radiation. The energy of the interacting radiation determines the processes, which may occur in an atom or molecule exposed to the radiation. A molecule may undergo rotational, vibrational, electronic or ionization processes in order of increasing energy or scatter light in a Raman process [15].

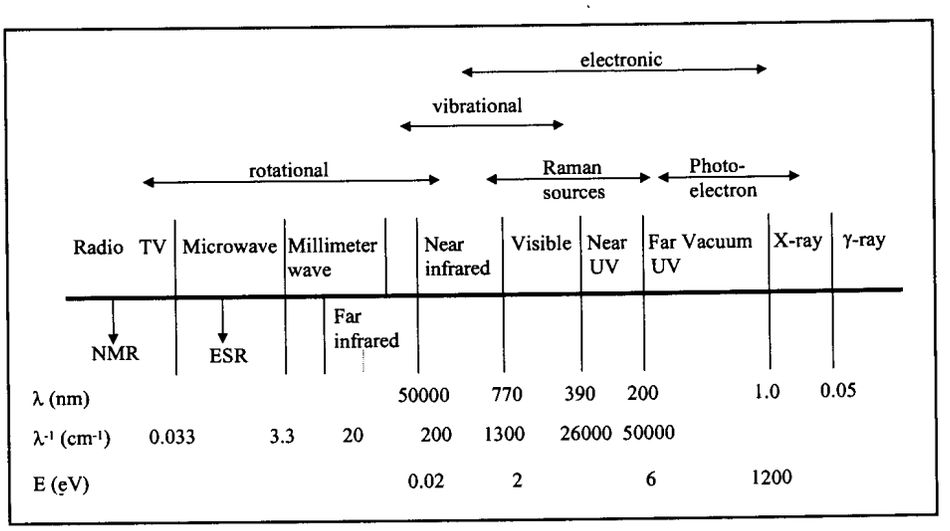

Figure 2.1: Regions of the electromagnetic spectrum

Raman and infrared spectroscopy measure the vibrational and rotational spectra of gases, liquids and solids. In the following section the basic principles of the two techniques are discussed in terms of the interaction with molecules and, since diamond and graphite are

crystalline solids consisting of atoms, which have no internal or rotational degrees of freedom, the lattice vibrations in crystalline solids will also be discussed.

2.1.1 The infrared experiment

Infrared absorption occurs when a photon incident on a molecule is absorbed and excites the molecule from the vibrational ground state to the next energy level, as illustrated in Fig. 2.2a. This transition is only possible if the energy difference between the two levels is

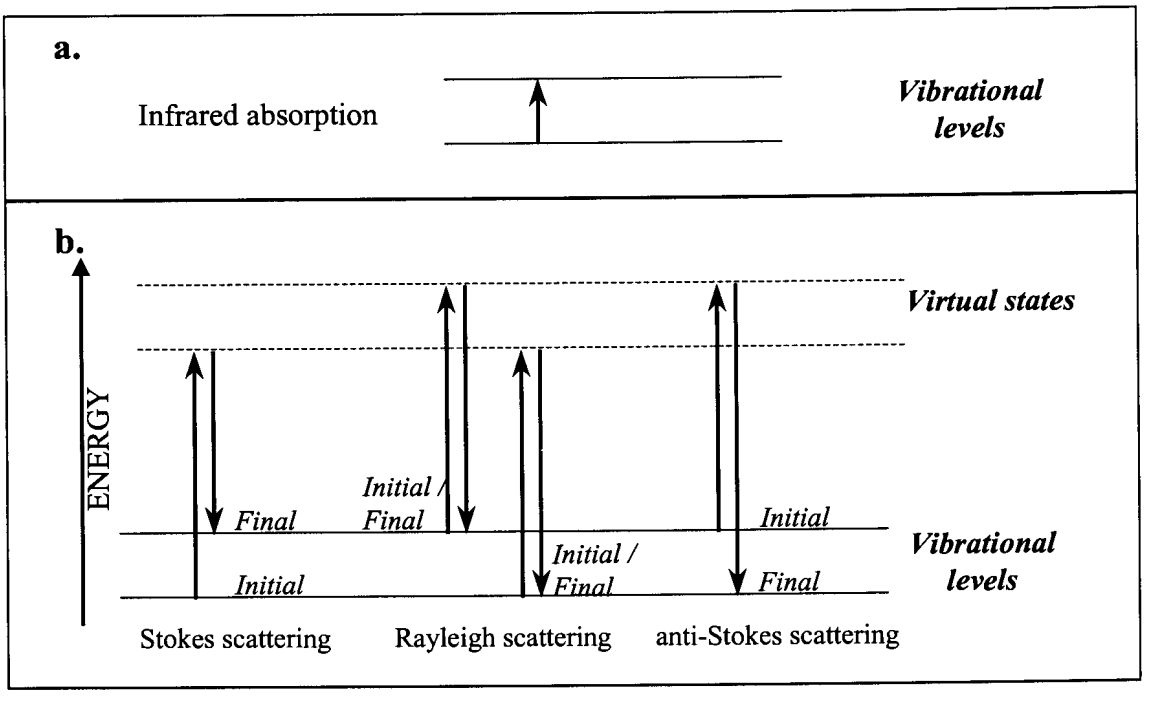

Figure 2.2: Illustration of the infrared absorption (a) and Raman scattering processes (b).

equal to the energy of the photon. A polychromatic source is therefore used to make a whole range of energies available for absorption. At frequencies corresponding to the fundamental vibrations of the sample some light is absorbed, while at the other frequencies the light is transmitted. The transmitted light intensity relative to the incident intensity is measured.

2.1.2 The Raman experiment

In a Raman experiment monochromatic light is scattered from the sample. Most photons are elastically scattered and have the same frequency as the incident photons (Rayleigh scattering). A small fraction of light (approximately 1 in 10^7 photons) is scattered at optical frequencies different from the frequency of the incident photons. The scattering is described as an excitation to a virtual state with nearly coincident de-excitation and a change in vibrational energy (Fig.2.2b). The energy difference between the incident and scattered phonons is shown by the arrows of different lengths in Fig. 2.2b and the energy difference between initial and final vibrational levels (ΔE), is calculated as follows:

$$\Delta E = hc\left(\frac{1}{\lambda_{incident}} - \frac{1}{\lambda_{scattered}}\right)$$

where h is Plank's constant, c is the speed of light and λ is the wavelength.

In chemistry it is customary to express the Raman shift in wavenumbers (cm^{-1}) and the frequency of a normal vibration (ν) is then:

$$\nu = \frac{1}{\lambda_{incident}} - \frac{1}{\lambda_{scattered}}$$

where, λ is the wavelength in cm.

At room temperature the population of vibrational excited states is low. Therefore, for the majority of molecules the initial state is the ground state and the scattered photon will have lower energy (longer wavelength) than the exciting photon (Stokes shift, Fig. 2.2b). According to the Boltzman population of states a small fraction of the molecules is in vibrationally excited states and Raman scattering leaves these molecules in the ground state. This type of scattering is known as anti-Stokes scattering and the scattered photon appears at higher energy (Fig. 2.2b) as the incident photons. The Stokes and anti-Stokes spectrum contains the same frequency information, but as the anti-Stokes shifted spectrum is always weaker than the Stokes-shifted spectrum the Stokes spectrum is what is generally used in Raman spectroscopy.

The laser lines used to excite Raman spectra are usually green, red or near-infrared. The wavelengths of these lines are well below the electronic transitions of most molecules or crystals, as assumed by scattering theory. If the wavelength of the exciting laser falls within the electronic spectrum of the sample the intensity of some Raman-active vibrations increases by a factor of 10^2-10^4 (resonance enhanced Raman scattering). The most common case is Franck-Condon enhancement in which a component of the normal coordinate of the vibration is in a direction in which the molecule expands during an electronic excitation. The more the molecule expands along the axis when it absorbs light, the larger the enhancement factor. The totally symmetric in-plane breathing modes of ring structures fall in this category [16].

2.1.3 Raman or infrared activity of vibrations

A molecule with N atoms needs 3N displacement coordinates to fully describe all possible motions. This includes three rotations and three translations and the number of internal vibrations for a molecule is therefore 3N-6 (3N-5 for linear molecules). Not all of the normal modes of vibrations will be observable as a band in the IR or Raman spectrum. The fundamental differences between the two processes determine the selection rules, which determine the Raman or infrared activity of a normal mode of vibration.

Interaction of infrared radiation with a vibrating molecule is only possible if the electric vector of the radiation field oscillates with the same frequency as the molecular dipole moment. A normal vibration is infrared active only if it alters the molecular dipole moment, that is:

$$\left(\frac{\partial \mu}{\partial q}\right) \neq 0$$

where μ is the molecular dipole moment and q stands for the coordinate describing the motion of the atoms during a normal vibration.

A similar condition must be fulfilled for a vibration to be observed in the Raman spectrum. When a molecule is exposed to an electric field, a dipole moment is induced which is proportional to the electric field strength and to the molecular polarizability α. A molecular

vibration can only be observed in the Raman spectrum if it alters the molecular polarizability, so that

$$\left(\frac{\partial \alpha}{\partial q}\right) \neq 0$$

If the conditions of the equations above are fulfilled by symmetry, then the vibrations are allowed or active in the infrared and Raman spectra respectively; if they are not fulfilled by symmetry, they are forbidden or inactive [16].

Several authors have outlined group theoretical methods, by which the symmetries of the normal modes of vibration of molecules and crystal lattices can be determined [17-20]. Character tables have been compiled to assist in determining the number of fundamental vibrations and the selection rules that govern its infrared and Raman activity.

The energy of a vibrational mode depends on molecular structure and environment. Atomic mass, bond-order, molecular substituents, molecular geometry and hydrogen bonding affect the vibrational force constant which dictates the vibrational energy. Force constants for crystal lattices are linear combinations of internal force constants and are a measure of the restoring forces experienced by atoms as they are distorted from the equilibrium position during a lattice vibration. The lattice force constant for diamond has been calculated as 4.7N/cm, which is in the same range as the force constant calculated for C-C in molecular compounds that is 4.4N/cm [16]. This means that the lattice vibrations of diamond occur in the same frequency range as the C-C bonds in molecular compounds.

2.1.4 Lattice vibrations in a crystal

A lattice, in contrast to a molecule, has an infinite number of vibrational degrees of freedom. The vibrations of the unit cell are regarded as being representative of all these motions and the infinite number of vibrations results from the different phases of the motions in the neighbouring cells, leading to a propagating wave [16]. Phonons are the quanta of energy in these elastic waves, corresponding to the possible vibrational modes of a crystal. A phonon is characterized by its wavevector $\boldsymbol{k}$, with the length of the wave vector equal to $2\pi/\lambda$,

where λ is the wavelength [21]. The direction of $\boldsymbol{k}$ can be either parallel or perpendicular to the particle motions, giving rise to the following phonons:

a. Longitudinal phonons (L): vibrations in propagation direction

b. Transverse phonons (T): vibrations perpendicular to propagating direction

Phonons are further classified into optical and acoustic branches:

a. Acoustic phonons (A): lattice points vibrate in phase with electron cloud – no direct dipole moment

b. Optical phonons (O): lattice points vibrate out of phase with electron cloud – strong electrical dipole moment [22].

The energy of a phonon is $hc\varpi_K$, where h is Planck's constant, c is the speed of light and ϖ_K is the frequency representation used in infrared and Raman spectroscopy (units: cm^{-1}, the customary notation is ν in chemistry, chapter 2.1.2). The energy is therefore dependent on the length and direction of the wavevector and dispersion curves that relate the frequency ϖ_K

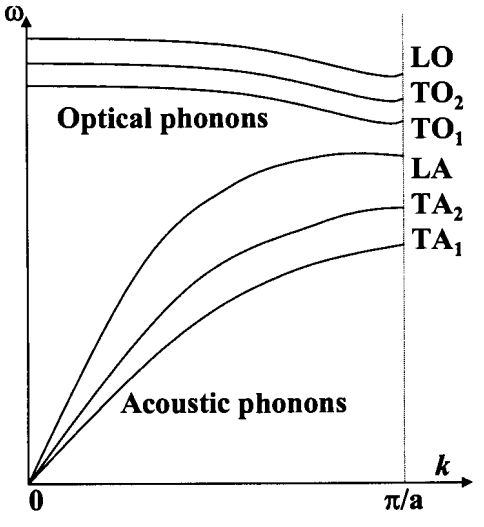

Figure 2.3: Typical phonon dispersion curves for the lattice vibrations of a three-dimensional anisotropic lattice with partial ionic bonding.

to the wavevector ($\boldsymbol{k}$) can be established, with the use of neutron scattering experiments. The exact relationship between ϖ_K and $\boldsymbol{k}$ depends on the masses of the atoms and elastic constant

of the crystal [21]. Where there is only one atom per unit cell, the phonon dispersion curves are represented only by acoustic branches. If there is more than one atom per unit cell a greater number of vibration modes is available and both acoustic and optical branches appear. Generally for a crystal with N-atoms per primitive unit cell there will be 3 acoustic branches (1 longitudinal and 2 transverse) and 3N-3 optical branches (N-1 longitudinal and 2N-2 transverse)

In Fig. 2.3 typical dispersion curves for a three-dimensional anisitropic lattice, with partly ionic binding and cell length a, is shown [24]. Only the first Brillouin zone, $-\pi/a \leq \boldsymbol{k} \leq \pi/a$, needs to be considered as values from outside only reproduce motions of atoms already described for $\boldsymbol{k}$ within these limits [21]. The two transverse modes are usually degenerate, but if a crystal is anisotropic the dispersion relations will be different for different directions in the Brillouin zone and the degeneracy between the two transverse modes for every $\boldsymbol{k}$ may be lifted [23]. In the isotropic cubic diamond lattice all the allowed modes are degenerate.

No change of dipole moment accompanies acoustic (LA) or optical (LO) modes and accordingly they are not infrared active (Chapter 2.1.3). Because the wavelength of light is long compared to phonon wavelengths, only the zone-center ($\boldsymbol{k} = 0$) phonons are observed in the single phonon (first-order) infrared spectra, as illustrated in Fig.2.3, but this is only true for ionic crystals where the electrostatic motions of opposite charges can produce the oscillating electric field with which the incident radiation can couple. Diamond, consisting of covalently bonded carbon atoms, therefore has no first-order infrared spectrum.

Multi-phonon absorption occurs when two or more phonons simultaneously interact to produce electric dipole moments with which the incident radiation may couple. This gives rise to a complicated second-order spectrum, which in the case of diamond is observed in the infrared spectrum.

Acoustic modes may be Raman-active, but at $q \approx 0$ they are extremely low in frequency (Brillouin scattering) and usually not observed in the Raman spectrum. In principle three Raman peaks can be observed due to the generation of optical phonons (TO_1, TO_2 and LO). They may be degenerate depending on the crystal symmetry and as with molecular vibrations group theoretical methods are used to predict the type and Raman or infrared activity of the

lattice vibrations. As a consequence of the high symmetry of the diamond cubic lattice all allowed modes are degenerate as already mentioned.

Similar to multi-phonon absorption a complex of phonons can be created together, giving a larger Stokes shift. In this case momentum can be balanced amongst the phonons and a wider range of energies is available to each phonon

2.2 Carbon and its allotropes

The electronic configuration of the carbon atom allows it to form a number of hybridized atomic orbitals, which have directional properties namely *sp* (digonal), sp^2 (trigonal) and sp^3 (tetragonal). The symmetry of the hybridized orbitals dictate the various ways in which carbon atoms bond to each other covalently, by the sharing of electron pairs. This in turn gives carbon the ability to adapt into various molecular and crystalline structures and the nature of these bonds underlies the varied chemical and physical properties of the carbon allotropes.

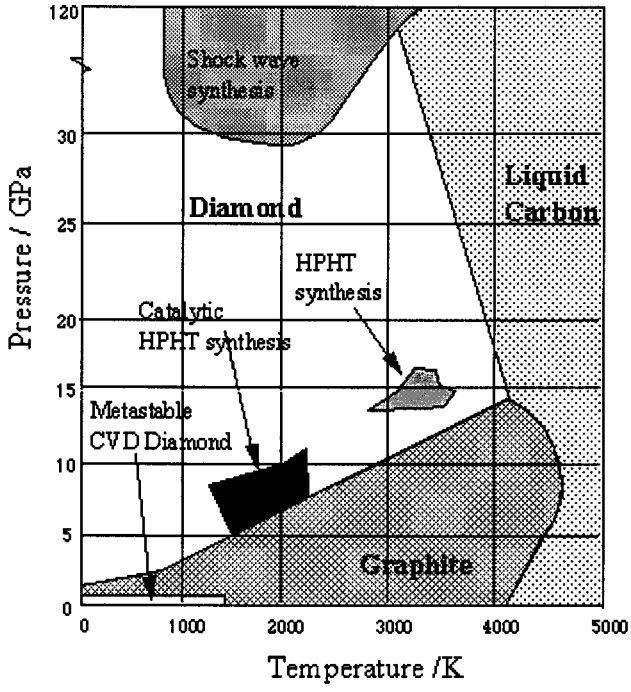

Figure 2.4: The phase diagram of carbon

These allotropic solids can be classified into three major categories:

a. sp^3 structures which include diamond and its polytypes, as well as polycrystalline diamond (CVD films)
b. sp^2 structures such as graphite, the fullerenes and carbon nanotubes
c. sp^2/sp^3 structures such as amorphous carbon, amorphous diamond and amorphous graphite, various other materials such as DLC (diamond like carbon), glassy carbon, etc.

Graphite is the stable form of carbon at room temperature and transforms into diamond at a temperature of approximately 3000 K and pressures above 1.25 GPa (in the absence of catalysts) as seen in the phase-diagram of carbon (Fig. 2.4). Diamond, being metastable, amorphizes easily even at room temperature when bonds are damaged or broken as happens when a diamond crystal is implanted with energetic ions. However, this damage can be annealed out if the damage level is kept below a critical value. Above the critical damage level annealing graphitizes the incurred damage.

The high cost of natural single crystal diamonds or HPHT (high pressure, high temperature) produced diamonds makes it impractical to use in commercial applications and therefore a CVD (chemical vapour deposited diamond) diamond sample was also included in this study to compare with the single crystal samples. The low temperatures and pressures used in the manufacturing of CVD or polycrystalline diamond (Fig. 2.4) are making it commercially viable to mass-produce.

The number and position of bands in Raman and infrared spectra depend on the symmetry and force constants of the bonds involved. Therefore the different crystal structures and bonding possibilities between carbon atoms in the different allotropes would yield different vibrational spectra that can and have been used to distinguish between the various forms of carbon. In the following section the Raman and infrared spectra of diamond and graphite, the two crystalline forms of carbon of relevance to this study, will be discussed. Also, the structure and vibrational spectra of the other two crystalline forms of elemental carbon namely fullerenes and carbon nanotubes will briefly be addressed, to illustrate the variety of bonds that carbon can form and the consequent influence on the properties and

vibrational spectra of the materials. As this study is mainly an investigation into the transformation of the rigid sp^3 configuration of carbon to the sp^2 configuration (illustrated in Fig. 2.5), the Raman spectra of various sp^2 bonded carbon materials i.e. amorphous graphite

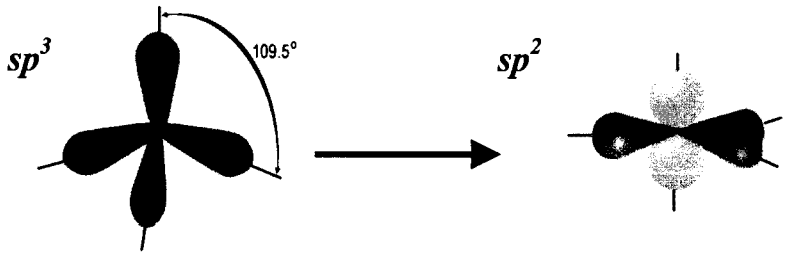

Figure 2.5: The configuration of the two most important hybridized atomic orbitals of carbon: sp^3 as in diamond and sp^2 as in graphite

(a-C_G), amorphous carbon (a-C_C) and other organic substances with sp^2 bonding will also be discussed.

2.2.1 The Raman and infrared spectra of diamond

In the rigid three-dimensional network of the diamond crystal the bonding electrons are held rigidly in localized tetrahedrally-orientated covalent bonds. This structure is responsible for the outstanding properties of diamonds, some of which are listed below:

- It has the highest thermal conductivity of any solid at room temperature
- It is the ideal optical material capable of transmitting light from the far infrared to the ultraviolet
- It has an unusually high index of refraction
- It is by far the hardest known material
- It has extremely high strength and rigidity
- It has the largest bandgap of all semiconductors namely 5.5eV [25]

Diamond crystallizes in the cubic face-centered space group $Fd3m$ (O_h^7) with all the sp^3 bonded carbon atoms on sites with symmetry m3m (O_h). The sp^3 hybridization accounts for the tetrahedral symmetry of the four $2sp^3$ orbitals (Fig. 2.5) found in the diamond atomic structure. These orbitals are bonded to four other carbon atoms with strong covalent bonds (1.54Å) to form a regular tetrahedron with equal angles of 109° 28′ to each other as shown in Fig. 2.6 [7].

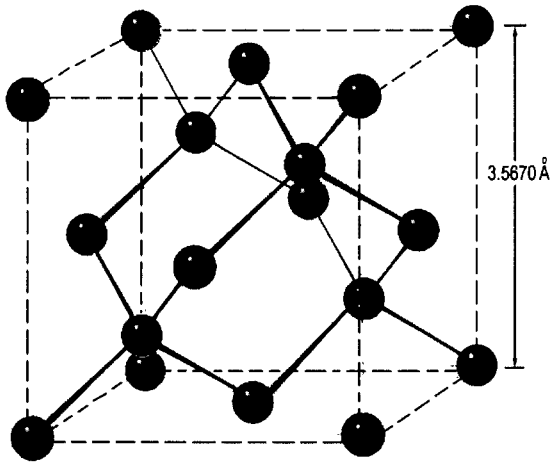

Figure 2.6: The cubic diamond crystal structure

There are two carbon atoms in the Bravais unit cell and a single triply degenerate first order phonon with symmetry T_{2g} is predicted from the selection rules of factor group O_h. This mode is Raman active only and the diamond structure has no first order infrared absorption. The first-order Raman band occurs as a thin sharp line at 1332 cm^{-1} with a halfwidth (FWHM) < 2cm^{-1}, as can be seen in Fig. 2.7.

The frequency of a Raman band can be considered, as a measure of the bond length between atoms and any distortion of the bond length due to stress/strain will produce a change in the vibrational energy or force constant (chapter 2.1.3). According to the pressure dependence curve of Sharma *et al* [26] a variation of 3 cm^{-1} indicates a variation in stress of 1.2 Gpa, which can be positive or negative (tension or compression).

The linewidth (FWHM) of the Raman band varies with the type of diamond sample and is also an indication of crystal quality. Some representative data is summarized in Table

2.1 [6]. It is clear from Table 2.1 that the FWHM of this peak is used to determine the crystal quality of diamond samples.

Table 2.1: Variation of linewith of Raman diamond peak in different samples (from ref 6)

Diamond Type	FWHM in cm^{-1}
CVD film, 900 °C, 1% CH_4, 60 Torr	7.4
CVD film, 980 °C, .5% CH_4, 60 Torr	5
Carbonado	2.7
Natural diamond	2
General Electric produced high pressure diamond	1.8

It has therefore become common practice to use this line as a measure of the quality of synthetic diamond structures namely: high pressure-high temperature diamond, CVD and DLC films.

Although diamond has no first-order infrared spectrum, it has a typical multi-phonon absorption between 1400-2350 cm^{-1}. Furthermore the infrared spectrum is very sensitive to the

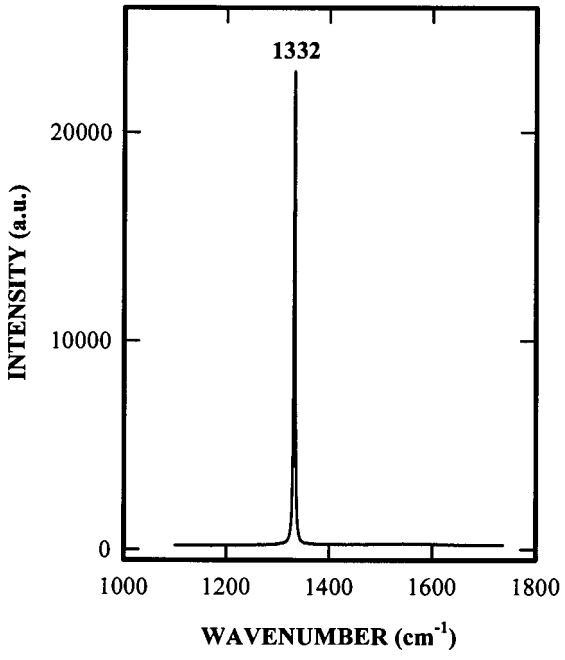

Figure 2.7: First order Raman peak

type of impurity present in natural, as well as synthetic diamonds and is used in the

classification of diamond into types. The classification of diamonds is summarized in Table 2.1 [25]

Table 2.2: Classification of diamond (from ref 25)

Type	Origin	Impurities
Ia	98% of all natural diamonds	~ 0.1% nitrogen in small aggregates Includes < 10% platelets Not paramagnetic
Ib	Rare in nature (<0.1%) Includes most high-pressure synthetic diamond	Nitrogen 0.05% in lattice Paramagnetic
IIa	Rare in nature	Few ppm of nitrogen Usually clear
IIb	Extremely rare in nature Produced by high-pressure synthesis	Less nitrogen than IIa Becomes semiconductor by boron doping Blue

A sharp peak at 1371 cm^{-1} in the infrared spectrum of diamond is an indication of nitrogen platelets in the diamond structure, while two broad bands at 1282 cm^{-1} and 1176 cm^{-1} have

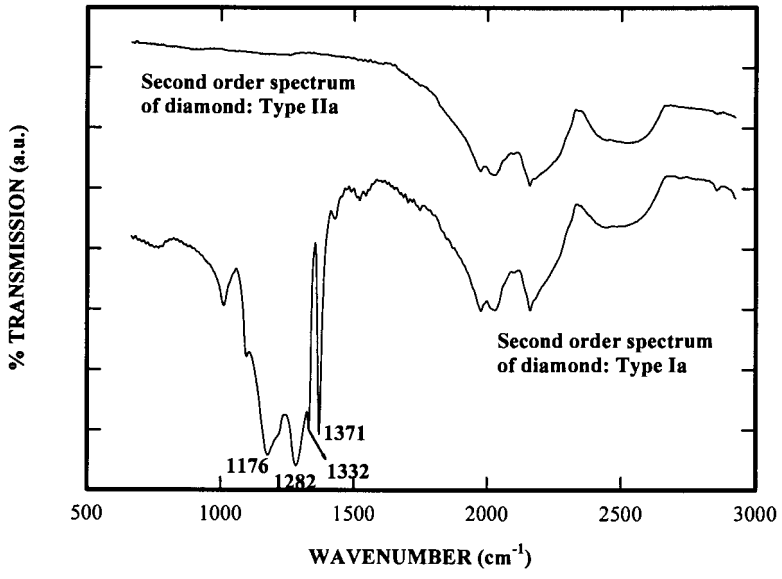

Figure 2.8: Second order infrared spectra of type IIa diamond (top) and type Ia diamond (bottom)

been attributed to nitrogen clusters [27]. The presence of these peaks is used to classify

diamonds according to Table 2.2 and the intensity of the peaks can be used quantitatively to establish the amount and type of nitrogen present in different samples [25]. The second order spectrum of Type IIa and Ia diamond can be seen in Fig. 2.8. The peaks due to nitrogen impurities are clearly visible, as well as the first order band at 1332 cm^{-1}. This band is usually not active in the infrared spectrum, but due to the distortion of the diamond lattice by the nitrogen inclusions, there is a relaxation of the selection rules, which makes this possible.

2.2.2 The Raman and infrared spectra of graphite

Single crystal graphite consists of flat layers in which the sp^2 bonded carbon atoms occupy the lattice sites of a two-dimensional hexagonal network. The layers are stacked in a hexagonal crystal structure corresponding to the space group $P6_3/mmc$ (D_{6h}^4) with Z=4 per unit cell. Interatomic distances between C atoms are 1.42 Å, with the distance between consecutive planes 3.354 Å. The carbon atoms are on sites *a* and *b*, each with site symmetry

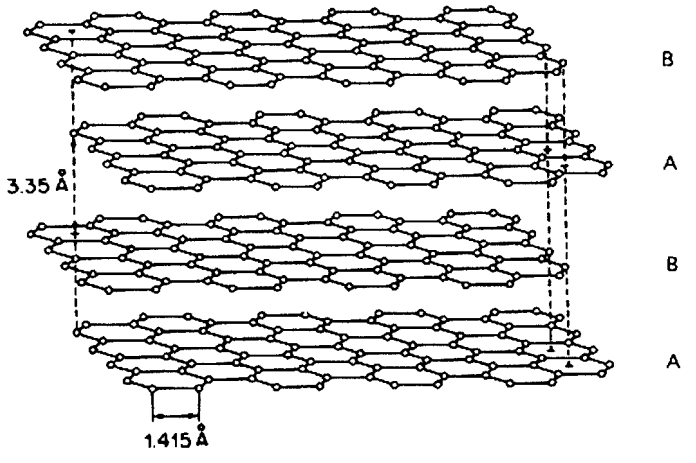

Figure 2.9: Graphite crystal structure

D_{3h} [28]. The much larger interatomic distance between sheets implies very little coupling between vibrational modes between sheets and the prediction of the normal modes (phonons) can be simplified to that of a sheet with a repeating unit of two carbon atoms. Using the correlation method, described by Fateley *et al.* [17], to predict the lattice vibrations, the site symmetry (D_{3h}) of the carbon atoms is correlated to the sheet symmetry (D_{6h}). As there are no

rotations in an infinite sheet two normal modes are predicted namely B_{2g} and E_{2g}. Only the E_{2g} mode is Raman active and no infrared absorption is predicted.

In Fig. 2.10 the Raman spectrum of a commercial graphite sample is presented. The most intense peak is at 1580 cm^{-1} and this belongs to the predicted E_{2g} mode. This mode, referred to as the *G* mode, is strongly dependent on in-plane displacements and is commonly used to characterize graphite-derived forms of carbon. For high quality single crystal graphite

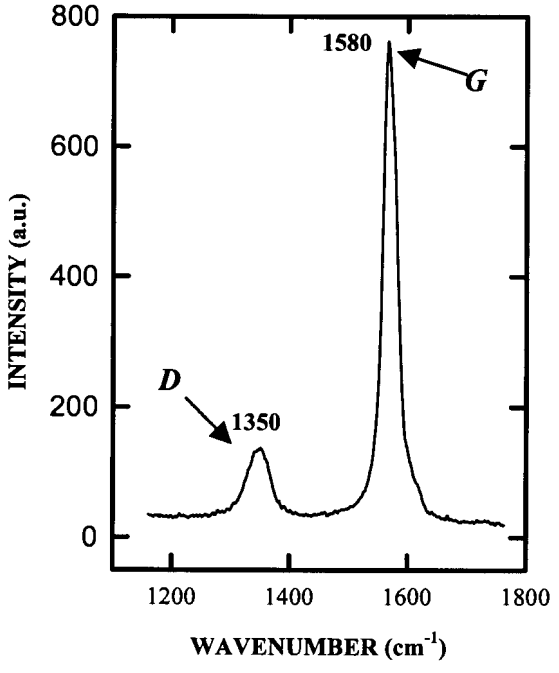

Figure 2.10: Raman spectrum of a commercial graphite sample

samples this is the only peak in the Raman spectrum. At 1350 cm^{-1} a small peak, known as the *D* mode (disorder induced), is visible in the commercial graphite spectrum, which is an indication that the sample is not a perfect single crystal. This is not surprising as the ideal hexagonal graphite structure described above is composed of theoretically infinite basal planes with perfect –ABABA- stacking and such an ideal structure is seldom found. The weak inter-plane bonds lead to numerous crystal defects such as vacancies, stacking faults and the random orientation of the parallel planes (turbostatic). The intensity of this peak is an

indication of the perfection of graphite crystals and will be further discussed in the section on amorphous carbon (chapter 2.2.4).

The delocalized electrons in the π orbitals are free to move in the direction of the graphite sheets, making graphite an electrical conductor in this direction. The relative large spacing between sheets makes it difficult for electrons to move from one plane to the other and as a result graphite is an insulator in the direction perpendicular to the graphite sheets.

2.2.3 The Raman spectrum of fullerene and carbon nanotubes

Fullerene and carbon nanotubes are included in this discussion to show the large variation of structures that sp^2 bonded carbon atoms can adopt and the resultant influence on the infrared and Raman spectra. C_{60} is the best-known fullerene and will be taken as example.

The 60 carbon atoms are located at the vertices of a regular truncated icosahedron, where every site is equivalent to every other site (Fig. 2.11). The average C-C bonding

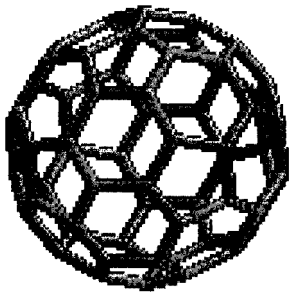

Figure 2.11: C_{60} fullerene molecule or "Buckey ball"

distance (1.44Å) is almost identical to that of graphite (1.42Å) and similar to graphite the C atoms are trigonally bonded to three other C atoms. The icosahedron has 20 hexagonal faces and 12 additional pentagonal faces to form a closed shell. Although the carbon atoms are all on equivalent sites, the three bonds originating at each carbon atom are not equal. Two of the bonds are electro-poor single bonds, while one is an electron-rich double bond, with bond

lengths 1.46 Å and 1.40 Å respectively. The inclusion of a five-membered ring between the hexagons is the cause of the rounded structure of the molecule [29].

To account for the bonding of the carbon in the fullerene molecule the hybridization must be a modification of the sp^3 hybridization of diamond and the sp^2 hybridization of graphite. Instead of the tetrahedral symmetry of the C atoms in diamond and the planar symmetry in the graphite sheet the bonds emanating from each carbon atom have pyramidal symmetry. The pyramidization angle and the nature of hybridization have been related to each other, with the σ character of the π orbital increasing with increasing angle [25].

Because of the high symmetry of C_{60} (point group I_h) there are only 46 distinct molecular mode frequencies corresponding to the 180-6=174 degrees of freedom for the isolated fullerene molecule. Four are infrared active and 10 are Raman active and the rest are silent modes. The most prominent Raman band at 1469 cm^{-1} is assigned to vibrations of the five-membered ring and the lower frequency, compared to the double bonds in the six-membered ring around 1570 cm-1, reflects the single bond character of the longer bonds in the ring. Less intense bands occur at 1248, 1318, 1426, 1573, 1575 and 1632 cm^{-1} [29].

The Raman spectrum of fullerene reflects the molecular vibrations of the molecules, as interaction between molecules are very little and at room temperature rotate freely around all three axes.

In the wake of the discovery of fullerenes carbon nanotubes were discovered in 1991. The one-dimensional carbon nanotubes refer to long carbon cylinders of nanometer dimensions (Fig. 2.12). The atomic arrangement of carbon atoms along the cylinder is like that of a rolled-up single layer of crystalline graphite (graphene sheet) and is capped by half a fullerene molecule at both ends of the cylinder. The hybridization of the sp^2 bonds is similar to that described for the fullerene molecule, with slight variations.

The most remarkable feature of the nanotubes is their ability to exhibit either metallic or semiconducting electrical properties depending on their geometry, which is a function of tube diameter and chiral angle (the chiral angle is described by the angles that the unit vectors of the graphene sheet make with the respect to the axis of the cylindrical nanotube). Important to this study is the fact that it is possible to use Raman spectroscopy to distinguish between the metallic nanotubes and the semiconducting ones [29]. The main bands in the Raman spectra of

the nanotubes are the typical G (1530-1640 cm^{-1}) and D (1320-1400 cm^{-1}) bands occurring in graphite. A special feature of the metallic nanotubes is that the G band at 1593 cm^{-1} is resonance enhanced, broadens and shifts to lower wavenumbers (1540 cm^{-1}) for laser excitation lines with wavelengths between 550nm and 600nm [30].

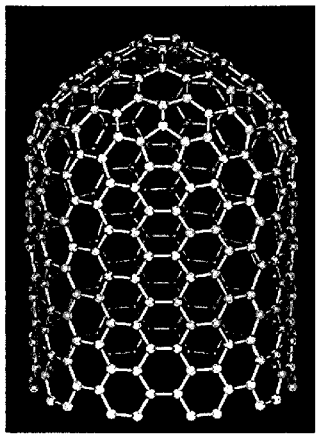

Figure 2.12: Illustration of carbon nanotube (from Rice University)

In studying the four crystalline forms of carbon it is clear that the directional properties of the sp^3 orbitals of carbon in the diamond crystal structure are the determining factor of the rigid crystal lattice with strong covalent σ bonds. In graphite the planar carbon sp^2 orbitals determine the flat sheet structure, which is responsible for the softness and metallic behaviour of graphite. These two crystalline solids each have very distinctive Raman spectra, which make it possible to distinguish between the two, using Raman spectroscopy. The bonding structures in the fullerene molecules and carbon nanotubes show that other directional possibilities exist for sp^2 bonding, which influence the characteristics and Raman spectra of the two solids. Of special note is the resonance enhancement of the tangential mode in the metallic nanotubes. It indicates that slight distortions in the atomic arrangement and consequent distribution of electrons in sp^2 bonded structures can have a huge influence on the conducting properties of the sample, as well as the observed Raman spectra.

2.2.4 The Raman spectrum of amorphous carbon

Apart from the four crystalline solids already discussed carbon forms a multitude of other natural or manufactured carbonaceous materials, consisting of varying mixtures of *sp*, sp^2 and sp^3 bonds. Examples are coal, chars and pitches occurring in nature and manufactured lampblack, vitreous carbon, carbon fiber and molded carbon. These are but a few of the vast large variety of carbon and carbon products, each with its own specific characteristics, which vary from ultrahard DLC (diamond-like) coatings to vitreous carbon foam.

The amorphous materials can be classified according to the ratio of sp^2 and sp^3 bonding present (the amount of *sp* is usually small). For the purpose of this study I will distinguish between amorphous diamond (a-C_D), amorphous graphite (a-C_G) and amorphous carbon (a-C_C).

The first Raman spectrum of amorphous diamond (a-C_D), a fully sp^3 bonded carbon network in the absence of aromatic sp^2 clusters, has been published only recently [31]. The Raman spectrum agrees closely with the calculated density of states and was obtained from amorphous sp^3 bonded nanoclusters produced deep inside a single crystal diamond with MeV ions. The deep implantation creates clusters within a largely intact diamond matrix, which maintains the clusters under high pressure, preventing the relaxation to sp^2-bonded structures. The spectrum consists of the first order Raman peak, which has broadened and shifted to 1200 cm^{-1}. An important feature is the absence of any bands around 1500 cm^{-1}, which would indicate the presence of sp^2 structures.

As seen in Fig 2.10, a modest amount of disorder in graphite can give rise to the peak at ~1350 cm^{-1} in the Raman spectrum of graphitic materials, which is not present in the Raman spectrum of single-crystal graphite. Tuinstra and Koenig [28] explained the appearance of the band as a consequence of the relaxation of the full D_{2h} symmetry of the graphite sheets in finite crystals. They then linked the crystal size of the graphite crystals in a sample to the inverse of the intensity of this band, which they called the *D* band (disorder induced). This has led to the so-called Knight formula,

$$L_a = C(I_D/I_G)^{-1}$$

where L_a is crystallite size, *C* is a constant 44 Å and I_D and I_G the intensity of the *D* and *G* band respectively. The use of this formula to classify materials derived from carbon has

become common practice, and is used in industry to follow the evolution from carbonaceous material to graphite [32].

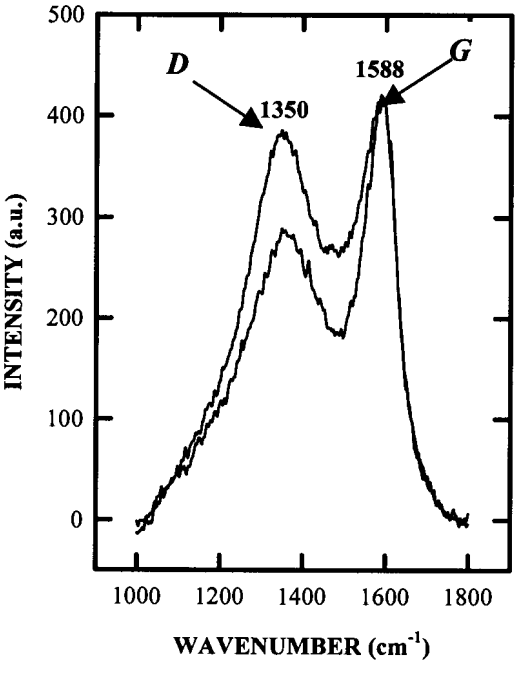

Figure 2.13: The Raman spectra of two commercial coke samples

Recently, it was shown that the origin of this peak is not due to laser-energy-independent features in the phonon-density of states, but to a resonance-enhanced Raman process caused by the coupling between electrons and phonons with the same wave vector near the k=0 point of the Brillouin zone. The position and intensity of the peak are thus dependent on the frequency of the exciting laser and in practical terms means that the Knight formula is only applicable for laser exciting lines near λ=514.5nm [33]. Not only is the position of the peak dependent on laser energy, but also on variation in the structure of each material. This has resulted in a great variation in the exact position of the bands quoted in the literature.

In Fig. 2.13 typical spectra of amorphous graphitic material are presented. The *D* and *G* bands, as observed in the spectrum of commercial graphite (Fig. 2.10) are present, but broadened and the intensity of the disorder-induced peak at 1350 cm^{-1} (*D* band) has increased,

as expected. There is no clear distinction between amorphous graphite and amorphous carbon, but a spectrum with two distinct peaks around 1350 cm^{-1} (*D*) and 1580 cm^{-1} (*G*) can be considered as amorphous graphite. It is assumed that in such a structure most of the carbon atoms are sp^2 bonded into six-membered rings as in graphite, but stacking disorders and crystallite size are responsible for the deviation from the perfect graphite crystal structure.

In between the two amorphous forms (a-C_D and a-C_G) discussed above, a wide range of materials exists which can be classified as amorphous carbon. Although the exact structure of amorphous carbon (a-C) cannot be determined, various theoretical models have attempted to describe the structure [34-38]. If the carbon is mostly sp^2 bonded it is believed that the structure exists of five, six and seven-membered rings cross-linked to each other by fractions of *sp* and sp^3 atoms present in varying amounts. As curvature is introduced into the structure by five- (positive curve) and seven- (negative curve) membered rings intermediate hybridization states similar to that of fullerene and carbon nanotubes is adopted. This in turn is responsible for varying C-C bonding distances and degrees of delocalising of π electrons, which have an influence on the Raman spectra of the materials.

This rich variety of structure is further extended as the concentration of sp^3 sites is increased so that they become dominant. The essentially layered material progressively changes into the dense isotropic network of mostly tetrahedrally bonded carbon, sometimes referred to as ta-C [30]. This highly tetrahedral form of carbon shows electronic, optical and mechanical properties, which approach those of diamond and is indeed sometimes referred to as amorphous diamond or diamite [7].

Both these forms of a-C are characterized in their Raman spectrum by one broad band with a maximum between 1400-1600 cm^{-1} and are distinctive from the Raman spectrum of a-C_G with its typical *D* and *G* bands. The only way to distinguish between the forms is the position of the peak maximum and it has been found that an increase of sp^3 sites shifts the peak to higher frequency values as the sp^2 bonds become isolated and the π electrons more localized [34, 39, 40].

For the purposes of this study I shall only differentiate between a-C_G, a-C_C and a-C_D, as a different Raman spectrum is associated with each configuration. Together with the distinct Raman spectra of crystalline diamond (c-C_D) and single crystal graphite (c-C_G) it is

clear that Raman spectroscopy is an excellent tool for studying the radiation damage in diamond materials.

2.2.5 The Raman and infrared spectra of polycrystalline diamond

As already mentioned a polycrystalline diamond sample was also investigated, as this would be the logical choice for any industrial application. The processes of producing low-pressure chemical vapour deposited diamonds (CVD) have improved in recent years and polycrystalline diamonds with properties very similar to that of single crystal diamonds are produced. Over the years both Raman and infrared spectroscopy have played a major role in monitoring the quality of the samples and thus optimizing the production processes.

Infrared spectroscopy is very sensitive in detecting the presence of C-H, C=O, N-H and other bonds originating from the aliphatic and aromatic precursors used to vapour-deposit the diamond [8, 9, 40-42]. Raman spectroscopy is used to monitor the diamond crystal quality and to detect amorphous carbon or graphite in the samples as explained in the proceeding paragraphs [6, 10, 35, 39, 40 and 43]. In this study I have determined the crystalline quality of the CVD diamond used in our investigation with these methods.

2.2.6 The Raman spectra of the sp^2 carbon in other organic substances

Except for sp^2 bonding in the carbon materials already discussed sp^2 bonding occurs in other organic compounds as C=C double bonds and is observed in the region between 1500 cm^{-1} and 1900 cm^{-1}. The bands of isolated double bonds in unstrained chains are found between 1640 and 1680 cm^{-1}, but in "strained" ring systems, such as three-membered rings it varies significantly as can be seen in Fig. 2.14. It has been shown that the unusual position of the C=C double bond is a result of a strong mechanical vibrational coupling in a X-C=C-X system, with a highly obtuse X-C=C angle and not of tension in the ring [16].

The above-mentioned influence on the C=C bond frequency is not the only factor contributing to the great variation, but conjugation with other unsaturated groups shifts the C=C frequency to lower wavenumbers

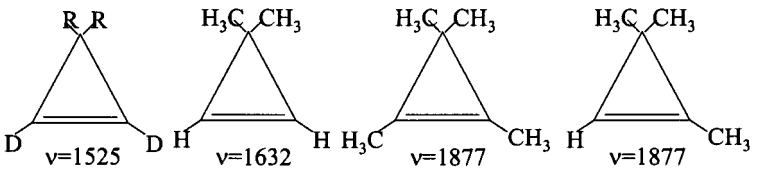

Figure 2.14: Variation of the position of C=C bonds (in wavenumbers) in three-membered rings.

In conclusion to this section, it is clear that the unique property of the carbon atomic orbitals to assume the three different hybridization states (*sp, sp*^{2} *and sp*^{3}), as well as modifications there-of, has led to the formation of a wide range of materials. The Raman spectra associated with each of these materials display unique properties. The $\pi \rightarrow \pi^*$ transitions associated with the delocalised electrons of *sp*^{2} bonding are responsible for a resonance enhancement of some of the Raman bands, which make the detection of very small amounts of *sp*^{2} bonding possible. The Raman spectra of the four ordered crystalline forms of carbon are governed by symmetry and the accompanying strict selection rules, but a slight deviation from perfect symmetry leads to a breakdown of the selection rules. The amorphous phases are a mixture of many different structures and with the loss of long-range order even isolated aliphatic-like bonds can be reflected in the spectra

2.3 Previous work on ion-implanted diamond samples

The large differences in the Raman spectra of the various forms of carbon (chapter 2.2) make the Raman technique particularly useful in distinguishing between one form of carbon and another. In ion-implantation studies of diamond, graphite and fullerene it has been used successfully to study the different variations of radiation damage caused by the incident ions, which can be directly related to the implantation process itself [11-14, 44-45].

It has already been mentioned that diamond implanted with ions at very high MeV energy levels yielded a Raman spectrum that has been attributed to amorphous diamond (chapter 2.2.4). In the same study extra peaks were observed at 1451, 1498 and 1634 cm^{-1},

which were attributed to defects and vacancies in the diamond lattice caused by the high-energy implantation. This is in contrast to other studies, where radiation damage caused by lower energy implantation resulted in Raman spectra displaying the broad band around 1500 cm^{-1} associated with amorphous carbon.

The resistivity in diamond drops upon ion implantation and diamonds with an electrically conductive surface layer can be used in many applications such as electrodes in electrochemistry. The electrical properties are dependent on the structure and chemical states of the implanted layer and the Raman spectroscopy has been used to find a link between the conductivity and type of radiation damage [45]. The samples studied, all displayed the broad peak around 1500 cm^{-1} associated with amorphous carbon. The spectra were deconvoluted into three peaks (1360 cm^{-1}, 1585 cm^{-1} and ~1500 cm^{-1}) using Gaussian distributions and it was found that an increase of the intensity of the peak around 1500 cm^{-1} indicated an increase in resistivity.

Although it is generally acknowledged that Raman spectroscopy can be used to detect very small amounts of sp^2 bonding in a sample, attempts to do it quantitatively have so far only been partially successful [35, 40].

CHAPTER 3

MEASURING TECHNIQUES AND EQUIPMENT

Infrared and Raman spectrometers usually combine a radiation source, a sample arrangement, a device for spectral dispersion or selection of radiation and a radiation detector, connected to appropriate recording and evaluation facilities [12]. In this chapter the two instruments used for conducting the experiments will be discussed.

3.1 Infrared instrument

A Bruker® 113v FTIR infrared spectrometer, linked to a computer equipped with OPUS software (also from Bruker®) was used to collect and analyze the infrared data. The instrument consists of the following three components.

3.1.1 The infrared source

The instrument is equipped with two infrared sources, namely a globar and a mercury arc (50-600 cm^{-1}), which make it possible to record spectra from 10-4000 cm^{-1}. The globar is the appropriate source for the mid-infrared region (400-4000 cm^{-1}) where the infrared spectrum of diamond was recorded.

The globar consists of a rod of synthetic silicon carbide, raised to a temperature of 1500 K by an electrical current and emitting continuum radiation approximating that of a black body. The instrument makes it possible to switch automatically from the one source to the other.

3.1.2 The Michelson interferometer

The central component of a FT-IR spectrometer is the interferometer, which acts as a dispersion element. In Fig. 3.1 the basic scheme of an idealized Michelson interferometer is

presented. Infrared light emitted by the source (S) is directed onto the beamsplitter (BS), which allows half of the light to pass through to the movable mirror (M2), while the other half is reflected to a fixed mirror (M1). The two beams are reflected at the mirrors and recombine at the beamsplitter. The infrared light reflected from the fixed mirror hits the beamsplitter

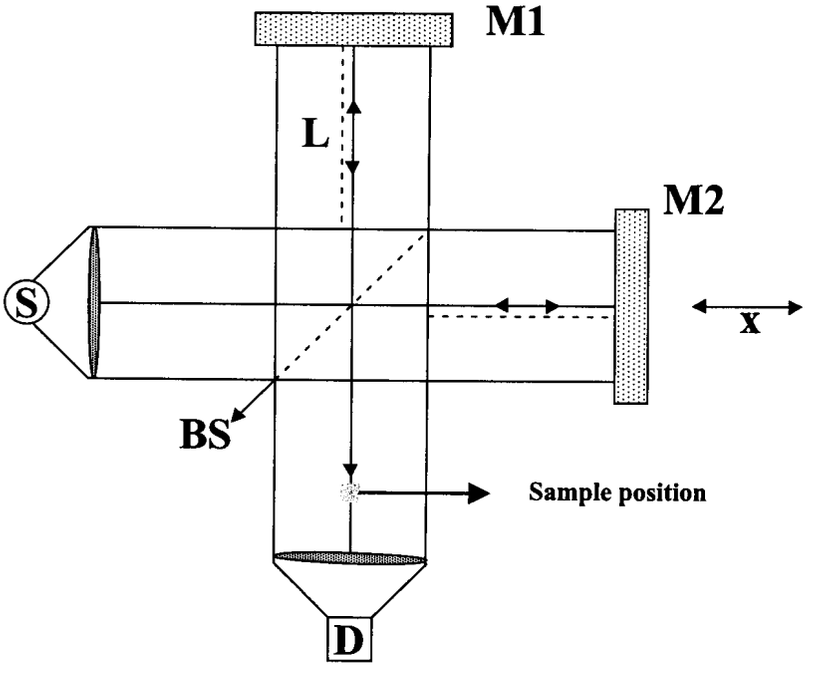

Figure 3.1: Schematic drawing of Michelson interferometer with S: source, D: detector, M1: fixed mirror, M2: movable mirror, X: mirror displacement and BS: beamsplitter

again after a distance of 2L. The reflecting mirror can move precisely back and forth around L by a distance x and on recombination with the reflected light has a path length of $2(L+x)$. Thus, when the two halves of the beam recombine on the beamsplitter, they exhibit a path length difference of $2x$, which means that the partial beams are spatially coherent and will interfere on recombination. The beam leaving the interferometer passes through the sample and is finally focused on the detector (D). The quantity actually measured by the detector is the intensity $I(x)$ of the combined IR beams as a function of the moving mirror displacement x.

The partial waves interfere constructively, yielding maximum detector signal if their optical retardation is an exact multiple of the wavelength λ, that is if

$$2x = n\lambda \ (n = 0, 1, 2, \ldots\ldots)$$

If $2x$ is an odd multiple of $\lambda/2$ destructive interference occurs, resulting in a minimum detector signal. The detector signal $I(x)$ is given by the cosine function:

$$I(x) = S(\nu)\cos(2\pi \nu x),$$

where the $\nu = 1/\lambda$ (wavenumber) and $S(\nu)$ the intensity of the monochromatic line located at the wavenumber ν.

Data acquisition yields the digitized interferogram (Fig. 3.2) $I(x)$, which is converted

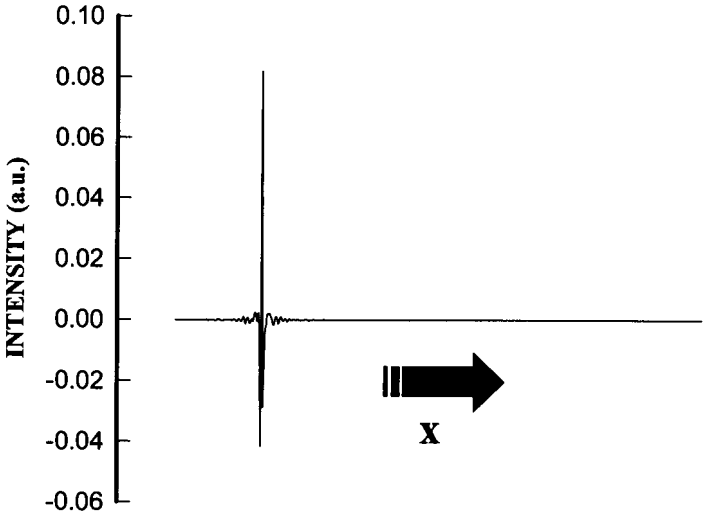

Figure 3.2: Interferogram

into a spectrum by means of the Fourier transformation. As the interferogram consists of N discrete equidistant points the discrete version of the Fourier transformation is used [46]:

$$S(k)k\Delta\nu = \sum_{n=0}^{N-1} I(n\Delta x)\exp(i2\pi nkIN)$$

where the continuous variables x and ν have been replaced by $n\Delta x$ and $k\Delta\nu$ respectively. The spacing $\Delta\nu$ in the spectrum is related to Δx by

$$\Delta\nu = 1/N\Delta x$$

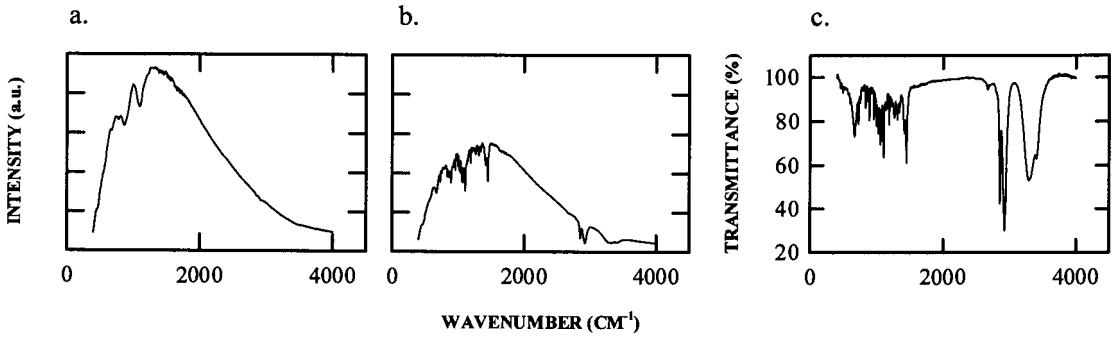

Figure 3.3: The single channel reference spectrum (a), single channel sample spectrum (b) and resultant transmittance spectrum (c)

The final transmittance spectrum is obtained in the following way:

a. an interferogram measured without a sample in the optical path is measured and Fourier transformed (single channel reference spectrum, $R(\nu)$ as seen in Fig. 3.4a

b. an interferogram with a sample in the optical path is measured and Fourier transformed (single channel spectrum, $S(\nu)$), Fig. 3.4b)

c. the final transmittance spectrum $T(\nu)$ is defined as the ratio $T(\nu) = S(\nu)/R(\nu)$

The Bruker 113v FTIR spectrometer contains a modification of the Michelson interferometer, namely the *Genzel* interferometer. Radiation from the source is focused on the beamsplitter and the transmitted and reflected beams are then collimated and passed in opposite directions to a double-sided moving mirror. This design makes it possible to use smaller beamsplitters, so that an automatic beamsplitter changer could be installed [47].

The radiation from a He-Ne laser is also passed into the interferometer and the sinusoidal interferogram measured simultaneously with the infrared signal acts as sampling trigger. The infrared interferogram is digitized at each zero-crossing of the laser interferogram. The advantage of this scheme is that the interferogram is measured at precisely equal intervals of retardation and all infrared wavenumbers are referenced directly to the laser wavenumber (15 804 cm^{-1}), imparting a high degree of accuracy.

It is vital that interferograms are signal-averaged coherently and to insure this radiation from a white light source is also passed through the main interferometer. The ~10 times shorter wavelength of the visible light causes the white light interferogram to be much sharper than the infrared interferogram. It is possible to set the zero retardation position of the white light interferogram to occur a few hundred micrometers before the zero retardation position of the infrared interferogram. When the intensity of the white light interferogram exceeds a certain threshold value, data-acquisition can be initiated by using the zero-crossings of the laser interferogram. Since the distance between the zero retardation position of the white light interferogram and the infrared interferogram remains precisely constant, coherent signal averaging is maintained over many thousands of scans [47].

3.1.3 Detectors

The instrument has two pyroelectric detectors to cover the mid and far infrared regions of the electromagnetic spectrum. The pyroelectric transducers are constructed from single crystal wafers of deuterated triglycine sulfate $(NH_2COOH)_3.H_2SO_4$). The incident infrared radiation causes a rise in temperature at the detector and the consequent change in polarization induces a voltage on the attached electrodes. Connections are directly to the electronic

circuitry without any intervening transformer. Switching between detectors is controlled from the computer [48].

The methods and parameters specified by the International Union of Pure and Applied Chemistry (IUPAC) that should be listed in publications are summarized in Table 3.1 [49].

Table 3.1: Parameters used during acquisition of infrared spectra

OPTICAL PARAMETERS	
Source	Globar
Beamsplitter	KBr
Aperture	10 mm
Detector	DTGS for mid-infrared region
Scanner velocity	10,51 KHz
Stabilization delay	0 s
Delay before measurement	0 s
Gain switch	OFF
Signal gain	Automatic

ACQUISITION PARAMETERS	
Laser wavenumber	15798 cm^{-1}
High frequency limit	8000
Low frequency limit	0
Interferogram size	14 K (3665 points)
Fourier Transform size	32K (8192 points)
Low pass filter	6.25 KHz
High pass filter	open
Acquisition mode	Single sided

FOURIER TRANSFORM PARAMETERS	
Phase correction mode	Mertz
Apodization function	Blackman-Harris 3-term
Zero filling factor	2
Phase resolution	128
Phase interferogram points	222

3.2 Raman instrument

A DILOR® XY modular system, which is composed of a spectrometer, multichannel detection, macro sample chamber, microscope (two entrances with optic fibre possibilities), electronic system and a computer were used during the experiments. The modular configuration makes it possible to expand the system and a foremonochromator was subsequently added to the system between rounds 2 and 3 (described in chapter 4) of ion beam irradiation. The λ = 514 nm Ar^+-ion laser from Coherent® was used as exciting line and a nitrogen cooled Wright® CCD camera used as detector.

3.2.1 The monochromatic coherent source

A laser (**l**ight **a**mplification by the **s**timulated **e**mission of **r**adiation) consists of three elements: an external energy source or pump, an amplifying medium and an optical cavity or resonator.

The Ar^+-ion laser used as exciting line during the Raman experiments is an Innova 300 supplied by Coherent® and functions in the following way:

A *population inversion* between two appropriate energy levels in the laser medium (Ar) is caused by electron impact in high current dc discharges.

Seed photons of proper energy and direction, caused by relaxation of ions at higher energy states to lower energy states along many possible relaxing routes, initiate the *stimulated emission* process.

An *optical cavity (Fabry-Perot resonator)* confines and directs the growing number of resonant energy photons back and forth between two mirrors through the laser medium, continually creating more stimulated emissions. A certain fraction of the laser light wave is directed outward through the output coupler mirror to form the external laser beam [50].

In Fig.3.4 the major energy levels of laser transitions in the Ar^+ ion laser are shown

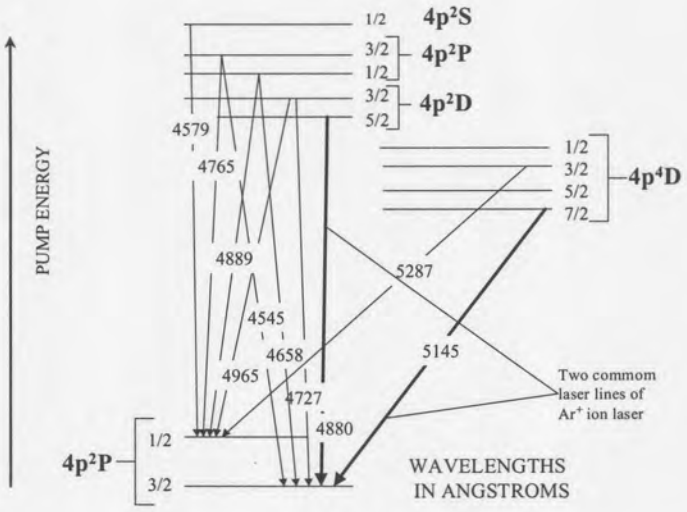

Figure 3.4: Energy level diagram showing major laser transitions in Argon II

[51]. The laser cavity forms a Fabry-Perot interferometer, which acts as a narrow bandpass filter. A combination of a wavelength selecting Brewster prism and etalon (a coated glass plate with parallel sides) inside the laser cavity ensures that the resulting laser beam has a narrow bandwidth and operates in the fundamental transverse mode (TEM_{00}), with a Gaussian distribution of intensity and propagates as spherical waves. In Fig. 3.5 the electric field across the transverse beam diameter for the fundamental TEM_{00} transverse mode can be seen, as well as the corresponding "burn pattern" [50]. This mode is obtained by limiting the divergence of the beam within the laser cavity.

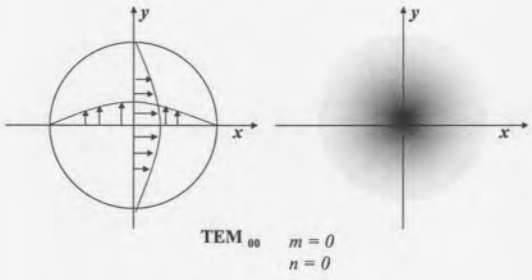

Figure 3.5: Gaussian distribution of laser line intensity in TEM_{00} transverse mode

3.2.2 The detector

A Wright® instruments nitrogen cooled CCD (charge coupled device) was used. The device is a photodiode array, which is a two-dimensional array of silicon p-n junctions.

A p-n junction is formed when n-type and p-type regions of semiconductors are in contact. In Fig. 3.6a the distribution of energy levels in p-type and n-type semiconductors is shown, with the Fermi level close to the valence band in the p-type and to the conduction band

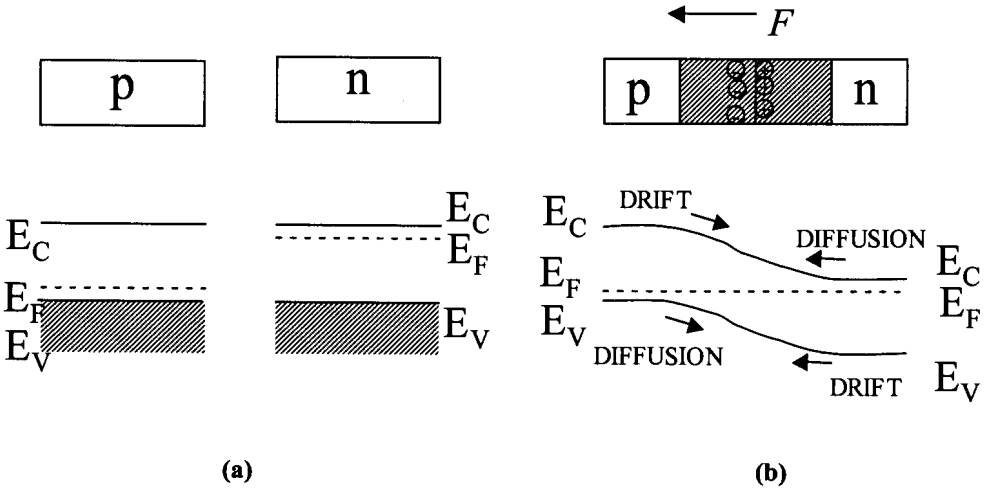

Figure 3.6: Uniformly doped p-type and n-type semiconductors before junction is formed (a), and the electric field (F) in the depletion region and the energy band of a p-n junction in thermal equilibrium

in n-type material. When the two regions are brought into contact, holes from the p-side diffuse to the n-side and electrons from the n-side to the p-side (Fig. 3.6b). An electric field (F) occurs as a consequence of current equilibrium [52]. Applying a voltage to a p-n junction the magnitude of the energy barrier is altered. Under forward bias the barrier height is decreased and under reverse bias increased. When a photon is absorbed in the region of the junction the electron-hole pairs are separated by the field causing a change in the voltage (*photovoltaic effect*) (Fig. 3.7). In an array of photodiodes each device responds to the incident radiation to provide one pixel (picture element) of output. On exposure to light each of the

devices stores photo-induced charge in a potential well. The number of electrons collected in a well is directly proportional to the number of photons incident on that pixel.

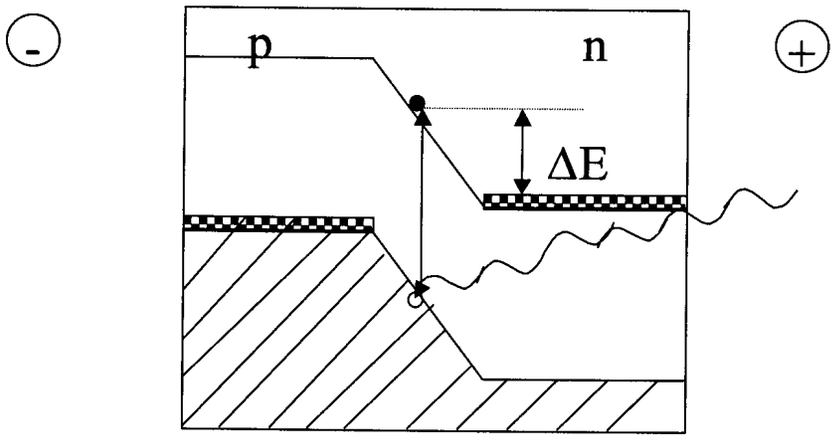

Figure 3.7: Operation of photodiode under reverse bias (adapted from ref 18)

In a CCD device, the charge must be moved from where it was collected to the edge of the chip where the readout amplifier is located. This movement is accomplished by using multiple adjacent gates. In a two-dimensional image array each row of wells is moved first up the chip and then one row at a time, across the top into the amplifier.

Charge readout speed and signal–to-noise are increased by binning. In binning, multiple wells are combined as they are moved to the serial register (the end channels on the chip that move charge laterally to the amplifiers). Because half as many charge packets must be read (for a 1 or 2 binning), the readout time is decreased as well as the effect of readout noise.

3.2.3 The spectrograph

For rounds 1 and 2 the spectrometer consisted of an asymmetric Czerny Turner (Fig.3.8) monochromator optimized by the computer for flat field and optical aberrations. The

Rayleigh scattered light is filtered before the entrance slit of the spectrograph by a notch filter (for a λ=514 nm line) placed in the optical path.

The incident light is directed by a plane mirror (PM) to the first concave mirror (CM1),

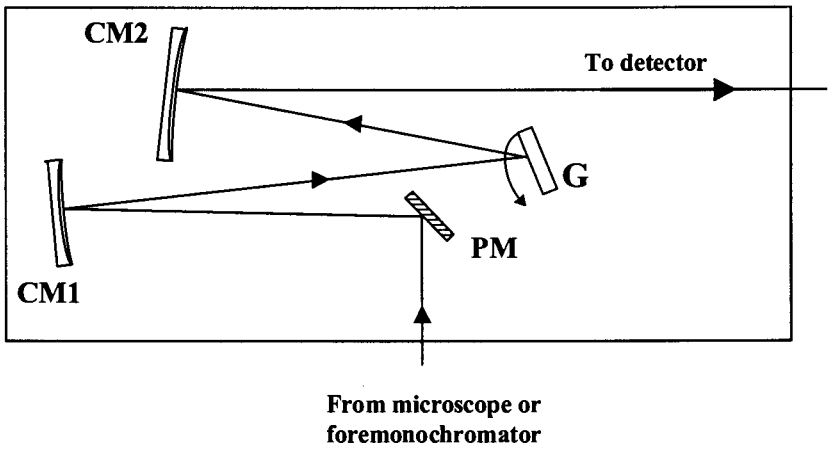

Figure 3.8: Czerny Turner with plane mirror (PM), two concave mirrors (CM) and holographic grating G

where the light is collimated and then incident on the grating (G). The light diffracted by the grating is incident on the second concave mirror (CM2), collimated and directed to the exit slit. The technical details are summarized in Table 3.2

Table 3.2: Technical details of spectrograph

SPECTROGRAPH	
Focal length of holographic mirrors	500 mm (600 mm for mirror to CCD exit)
Aperture	F/6
Holographic gratings	1800 gratings/mm (maximum efficiency at 500 nm)
Useful range	350 – 850 nm
Spectral range	30 500 – 11 200 cm^{-1}
Accuracy	2/10 000
Reproducibility	± 0.1 cm^{-1}
Grating drive	Cosecant drive, step 0.02 cm^{-1}

3.2.4 The foremonochromator:

After round 2 the Raman instrument was upgraded. A foremomochromator was installed before the spectrograph to replace the notch filter*, used in the previous setup, to filter the scattered Rayleigh radiation. The foremonochromator is a double monochromator, and as the spectrograph, it is a Czerny Turner mount consisting of four concave mirrors (focal length 800 mm). The XY modular system makes it possible to use the instrument in three configurations namely: double subtractive, double additive for high resolution work, or the foremonochromator can be bypassed and a notch filter inserted in the optical path.

The experiments for this study, after round 2, were recorded with the instrument in the double subtractive configuration (Fig. 3.9), where the foremonochromatoer selects a band pass and this signal is sent to the detector throughout the spectrograph. Two gratings are mounted on the same arm in a kinematic interchangeable holder. This cosecant arm, with a special high precision screw, is controlled by a linear encoder with a precision of 1 μm [53].

Slits S1 and S3 are identical, but independent and S3 determines the resolution of the spectrograph. S2 selects the band pass sent through to the detector and is open to 18 mm and

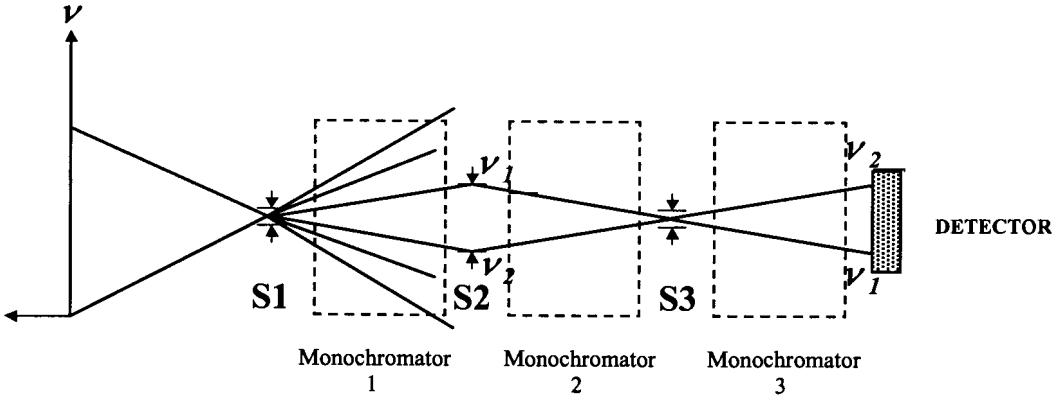

Figure 3.9: Arrangement of optical system in double subtractive configuration

adjustable around this value. The second stage is the image of the first one relative to the plane of the intermediate slit.

* A hologram operating as a wavelength-selective mirror

3.2.5 The camera

A monochrome video camera is attached to the microscope. The area on the sample which is to be analyzed is displayed on the video screen and a photographic record of the sample surface can be stored. In this study it was important to be able to record spectra on both the implanted and virgin parts of the samples, and the video camera made it possible to select the exact spot where the spectra were recorded.

3.2.6 The confocal microscope

All the Raman spectra for this study were recorded with the aid of a microscope attached to the instrument. The confocal design of the microscope allows rejection of much of the radiation originating away from the focal point. This is illustrated in Fig. 3.10 where it can

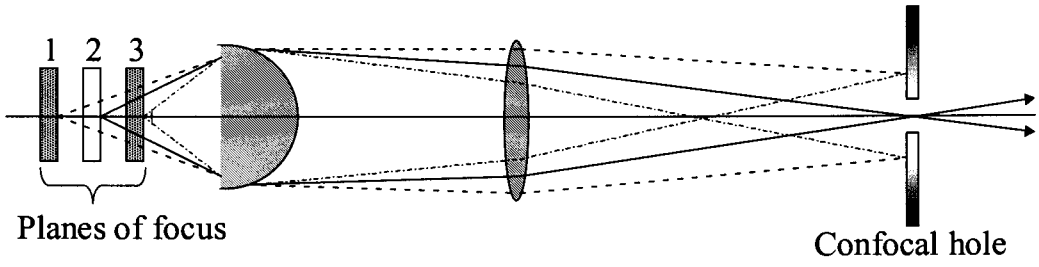

Figure 3.10: Only radiation originating from plane in focus (2) enters spectrograph trough confocal hole

be seen that most of the radiation from planes 1 and 3 does not pass through the aperture, because they are not focused in the confocal plane [53]. Thus, most of Raman and/or fluorescence radiation originating away from the sample depth of interest never reach the entrance to the spectrograph, so that the acquired spectrum is specific to the depth of the sample in focus.

The axial resolution of the instrument is a combination of both the distribution of laser beam irradiance along the z-axis and the spatial filtering by the confocal hole and explains the dramatic improvement of the axial resolution in a confocal arrangement [53].

The axial resolution describes the ability of the optical system to distinguish between adjacent thin sections Δz in the sample volume and can be controlled in a system by varying the magnification of the optical system, the numerical aperture of the objective and the dimension of the confocal hole. The axial resolution is then unique for a given set of parameters and in practice has to be determined for each sample under the specific recording conditions.

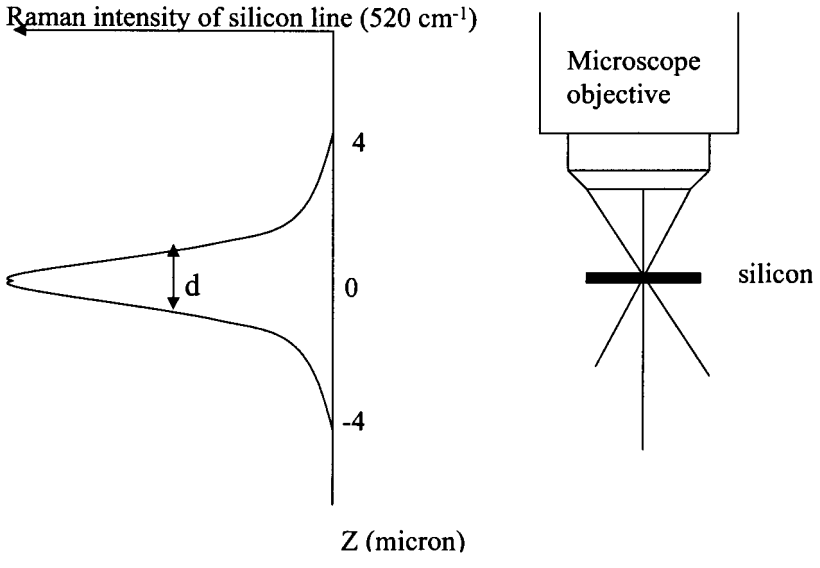

Figure 3.11: Experimental determination of the depth of focus for silicon.

In Fig. 3.11 it is shown how the axial resolution for silicon is determined. The intensity of the characteristic silicon line at 520 cm^{-1} is plotted versus the relative displacement along the z axes. The axial resolution or depth of focus d is defined as the FWHM of the Gaussian curve formed by the intensity distribution.

This important feature made is possible to record spectra of the thin layer of amorphous carbon formed under the surface of the diamond samples without too much interference from the diamond layer on top or beneath the damaged parts.

CHAPTER 4

EXPERIMENTAL PROCEDURES

Experimental procedures consisted of four rounds of ion-beam irradiation and thermal annealing steps on 5 natural single crystal diamond samples (16, 17, 18, 21 and 22). The crystal faces irradiated for each sample were as follow: 16 (111), 17 (110) and samples 18, 21 and 22 (100). A synthetic polycrystalline sample (X1), produced by chemical vapor deposition, was also investigated after round 4. Optical absorption, photo-thermal deflection, Raman and infrared, atomic force and ion-beam channeling measurements were taken after each step to monitor the induced phase transition from the crystalline to the amorphous state. The procedures for the Raman and infrared measurements are discussed below.

4.1 Irradiation with F = $3x10^{15}C/cm^2$

All five single crystal samples were irradiated with a fluence of $3x10^{15}C/cm^2$ (round 1) at energy 75 keV and temperature 77 K. One of the samples was annealed at room temperature and the others annealed for 1h at varying temperatures, namely 600, 900, 1200 and 1500 K. The samples were then analyzed using various Raman and infrared experimental techniques to determine the amount of damage incurred by the radiation and the effect of annealing at different temperatures on the damage.

Reflection infrared spectra were recorded of all five samples using a microscope attached to the FTIR instrument. This made it possible to record spectra on the irradiated part of each sample, as well as the virgin part. Transmission infrared spectra were recorded of all the samples pressed between two KBr pellets. In this instance no distinction could be made between the irradiated and virgin parts of the sample. As the irradiation was centered in the

middle of the samples it is assumed that the spectra reflect the properties of the damaged part of the samples.

Raman spectra were recorded on both the irradiated and virgin parts of each sample, with the aid of a confocal microscope (100x magnification) attached to the Raman instrument. The diameter of the analyzed area was ±12 μm, slit width 100μm, integration time 30s and laser power <25 mW at the sample. At least three spectra were recorded on different spots for each measurement to ensure representative sets of data.

4.2 Irradiation with F=0.3x10^{15}C/cm^2 and F=1.0x10^{15}C/cm^2

The procedures followed for round 1 were repeated, but fluences of 0.3x10^{15} C/cm^2 (round 2) and 1.0x10^{15} C/cm^2 (round 3) were used. Details of irradiation parameters used for rounds 1-3 are summarized in Table 4.1.

Table 4.1: Details of rounds 1 - 3: E = 75 keV, T_I ~ 77 K.

ANNEALING TEMPERATURE (K)		300	600	900	1200	1500
Round 1: 3.0x10^{15} C/cm^2;	sample#	18	16	17	21	22
Round 2: 0.3x10^{15} C/cm^2;	sample#	22	21	18	17	16
Round 3: 1.0x10^{15} C/cm^2;	sample#	16	17	18	21	22

Transmission FTIR spectra were recorded for all of these samples, using the same experimental conditions as in round 1.

The incurred damage (a-C formed) due to irradiation was much less in round 2 than in round 1 and, in order to observe any features due to a-C in the Raman spectra, the recording time for this region was increased to 200s. The diameter of the area analyzed was reduced to 2 μm as this decreases the depth of analysis and would therefore also favor the damaged part of the sample, which is close to the surface.

A notch filter was used during rounds 1 and 2 to block the Rayleigh radiation from the spectrograph entrance, but between rounds 2 and 3 a double subtractive monochromator was installed to fulfill the same function. The recording parameters were adjusted to produce spectra in the same intensity range as those previously recorded. The recording time for the region of c-D was reduced to 10s and for the region where bands can appear due to other carbon structures to 70s.

Between each round, the samples were etched in an oxygen plasma to a depth of about 10 μm to remove the introduced damage before starting the next round. Spectra of the virgin samples were also recorded to serve as reference spectra, after one of the cleaning procedures.

4.3 Irradiation through a metal grid

In round 4 irradiating the samples through a metal grid (Fig. 4.1) simulated data storage by creating "pixels" of spot size 7.5x7.5 μm^2, separated by 5.0 μm wide non-irradiated material. Experimental details are summarized in Table 4.2 [1]. All the samples were annealed at two temperatures, namely 300 and 1700 K (annealing time 5 min.). Raman and infrared spectra were recorded in the same way as for round 3.

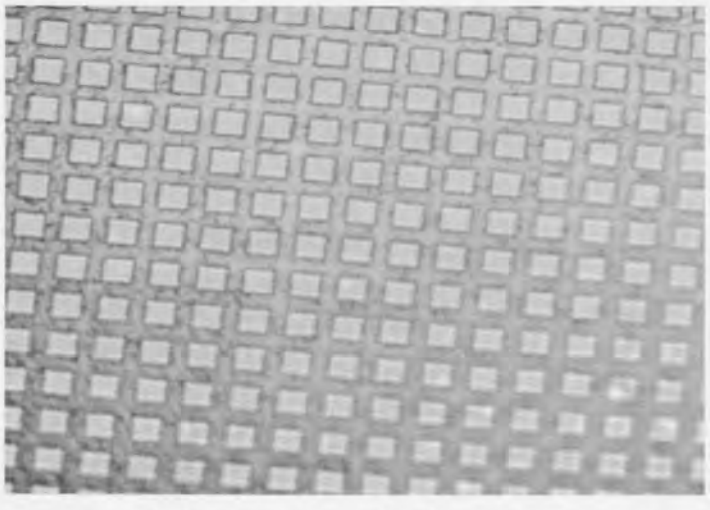

Figure 4.1: Video image of metal grid as seen with the x50 objective of the microscope

The damage created by the grid was visible in the video images of most of the samples and Raman spectra could be recorded on irradiated, as well as virgin parts of the samples.

Table 4.2: Details of round 4: E = 65 keV, $T_I \sim 77$ K, $T_A = 300, 1700$ K

Fluence [10^{15}C/cm^2]	0.1	0.3	1	3	10
Sample#	22	21	16, X1	17	18

CHAPTER 5

RESULTS AND DISCUSSION

In chapter 2 it was shown that diamond is characterized by the first order phonon, which appears as a single sharp peak at 1332 cm^{-1} in the Raman spectrum of a perfect diamond crystal. Variations in bond length and bonding angle (distortion from the perfect cubic lattice) influence the halfwidth (FWHM) and position of this band. For natural and synthesized diamonds the position of the diamond peak varies from 1331 to 1345 cm^{-1} and the FWHM from 1.8 to 15 cm^{-1}. Movement of the diamond peak to higher/lower wavenumbers is an indication of a compressive/tensile stress in the diamond lattice and an increased FWHM of this peak reflects an increase in structural disorder. Except for lineshift and broadening of the Raman peak at 1332 cm^{-1} the appearance of Raman peaks in the region between 1350 and 1700 cm^{-1} is an indication of disorder in diamond crystals (chapter 2.2.4).

The mid-infrared spectrum of pure diamond is dominated by two-phonon absorptions in the 1333-2666 cm^{-1} region, which are intrinsic to pure diamond (chapter 2.2.1).

5.1 Virgin samples

Infrared and Raman spectra of the 5 single crystal samples (16, 17, 18, 21 and 22), as well as the polycrystalline sample (X1), were recorded for use as reference spectra. The results are depicted in Fig. 5.1 and clearly show the presence of the two-phonon absorptions (1333-2666 cm^{-1}) that are intrinsic to diamond. In sample 22 these bands are quite weak compared to the other samples and in samples 21 and 22 extra bands between 1000 and 1400 cm^{-1} are observed due to nitrogen impurities. These bands are used to classify diamonds into different types and, according to this classification, samples 21 and 22 represent type Ia diamonds and samples 16, 17 and 18 type IIa diamonds (chapter 2.2.1).

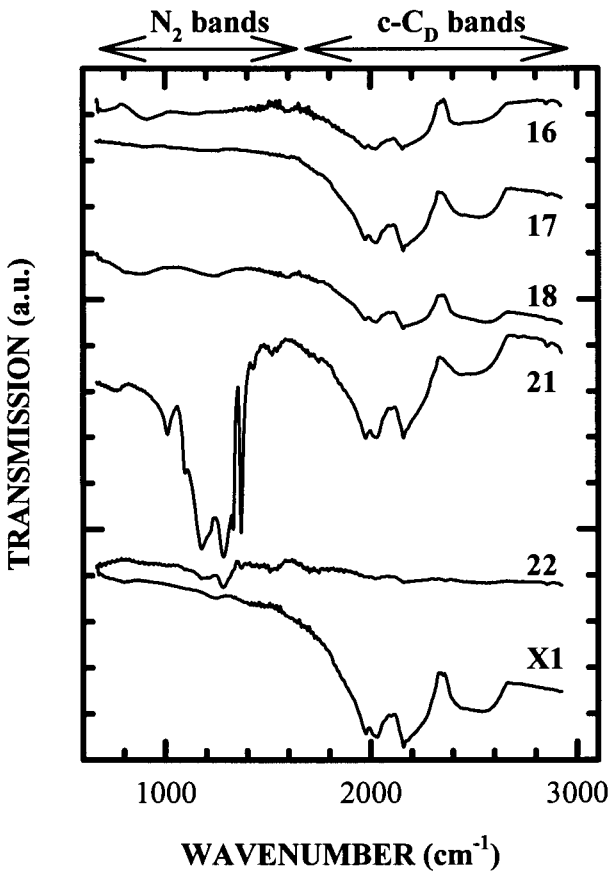

Figure 5.1 FTIR transmission spectra of virgin samples

The Raman spectra of the single crystal virgin samples all displayed the main Raman band at 1332 cm^{-1} as expected (compare Fig.2.7, chapter 2.2.1). The only difference between samples are intensity variations of this peak, and a closer analysis revealed slight differences in the FWHM of the same band; for samples 16, 17 and 18 the FWHM was < 2 cm^{-1}, but > 2.5 cm^{-1} for samples 21 and 22. This can be ascribed to the nitrogen impurities present in these two samples, as detected with the FTIR measurements (Fig.5.1).

The FWHM of the peaks were determined using the Labspec software obtained from Dilor®. The results were not corrected to compensate for overestimation caused by finite–slit effects [54], as the instrument resolution was <1 cm^{-1} throughout the measurements and it was believed that peak broadening was kept to a minimum.

The Raman spectra of the synthetic polycrystalline sample varied in the position (1330-1333 cm^{-1}) and FWHM (1.8-2.5 cm^{-1}) of the first order phonon. This is an indication of varying stress levels within the diamond lattice, which is common in polycrystalline samples [43, 55].

5.2 Irradiation with F = $3x10^{15}C/cm^2$.

In round 1 the main objectives were to establish an experimental procedure to monitor the transition from c-C_D to a-C_C. The effect of annealing at different temperatures and the possible transition to graphite under certain annealing conditions were also investigated.

5.2.1 Raman results

In Fig. 5.2 a representative spectrum of each of the c-C_D samples, F=$3x10^{15}C/cm^2$,

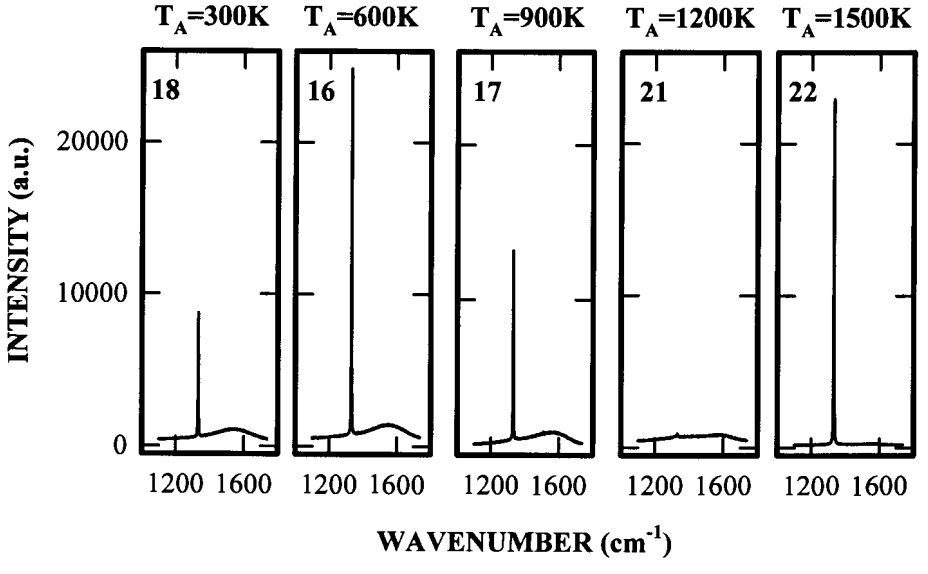

Figure 5.2: Raman spectra from round 1 plotted against the same scale

annealed at different temperatures, are plotted to the same scale. The most prominent feature in all of the spectra, except for c-C_D 21, is the sharp diamond peak at 1332 cm^{-1}. At T_A =1200K, the drop in the intensity of this peak is so drastic that it indicates a complete structural change in the c-C_D, but at T_A=1500K the peak has been restored to its original shape and intensity.

For T_A<1200K the intensity of this peak varies between the samples, but a trend, that could connect the intensity of this peak to annealing temperature, is not observed. As a variation of peak intensity was also observed between the spectra of the virgin samples it follows that for T_A<1200K the contribution of differences between the samples influence the peak intensity more than the amount of amorphous carbon present. Therefore the spectra were further analyzed to find another way to compare these spectra with each other.

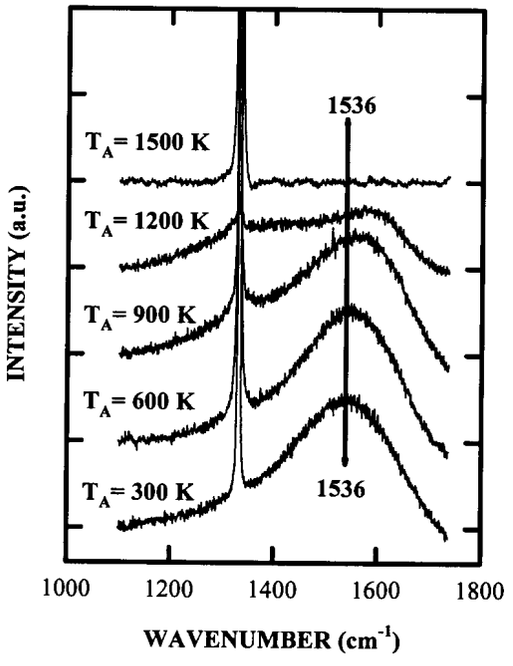

Figure 5.3: Raman spectra of samples in round 1 with a-C_C part of spectrum enhanced.

In Fig. 5.3 the same spectra depicted in Fig. 5.2 are plotted on the same axis and to a scale that enhances the disordered carbon part of the spectra. A qualitative inspection of the spectra shows that annealing between 300-900 K does not change the intensity of the broad

peak between 1400 and 1700 cm^{-1}, representing a-C, much. The position of the peak shifts to higher wavenumbers and becomes asymmetrical and at T_A=1500K there is no trace of any peaks in this region of the spectrum.

A polynomial fitting procedure was applied to all the spectra to resolve this broad band into the *D* and *G* bands generally used to determine the degree of graphitization of carbons (chapter 2.2.4). The spectra were not filtered or smoothed in any way and the deconvolution option of the Labspec software obtained from Dilor® was used for the fitting procedure. The program allows the fitting procedure to be done using a Lorentzian, a Gaussian or a Gaussian/Lorentzian mix function. All three options were tried, with the best results obtained in the order Gaussian/Lorentzian, Gaussian, Lorentzian, which is in agreement with Lee *et al.* [11], who also found that a mix-function gave the best results.

$$y = a\{g[\underbrace{\exp(-\frac{(x-p)^2}{\omega^2})}_{\text{Gauss}}] + (1-g)[\underbrace{\frac{\omega^2}{\omega^2 + 4(x-p)^2}}_{\text{Lorentz}}]\} \tag{5.1}$$

where a = peak height,

g = Gauss fraction,

p = peak position and

ω = peak width at half maximum

The fitting parameters were optimized iteratively with the method of maximum gradient. In each step (j) the deviation of the interpolation from the real spectrum is calculated summing over all spectral pixels.

$$d(j) = (I_f - S_f)^2 \tag{5.2}$$

where I_f = intensity at frequency f

and S_f = the value obtained at frequency f by the peak fitting.

The calculation terminates when $\left|\frac{[d(j)-d(j-i)]}{d(j)}\right| < 0.001$ (5.3)

In Figure 5.4 the deconvolution results of the samples annealed at 300 K and 1200 K respectively are displayed graphically and the data for all the samples are summarized in Table 5.1. The g-factor in equation 5.1 as determined by the fitting procedure is also shown in Table5.1 It is interesting to note that for the main Raman band a 70% Lorentzian curve was used in the fitting procedure, while for all the other peaks nearly 100% Gaussian curves were

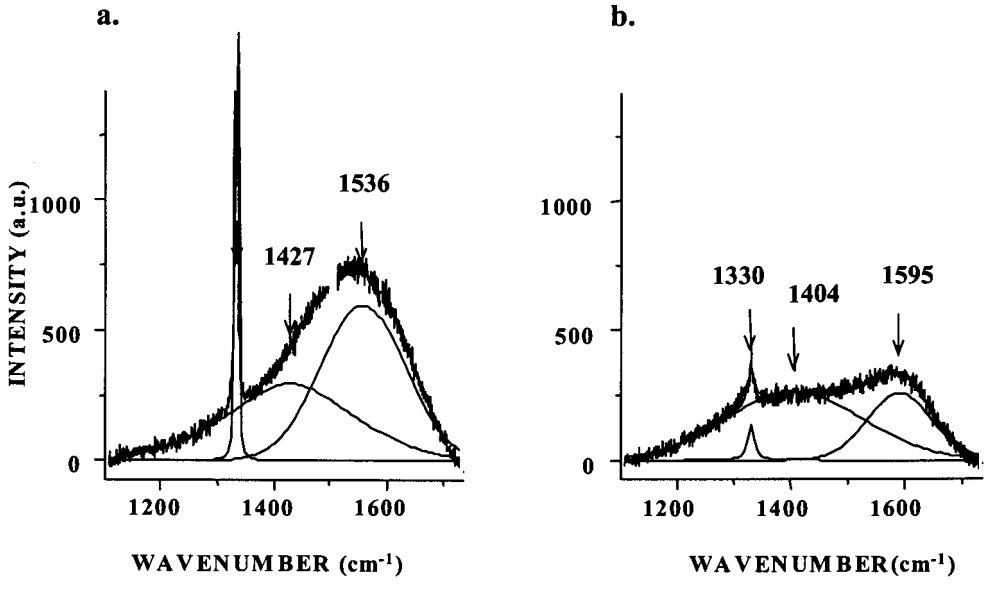

Figure 5.4: Deconvolution of samples annealed at (a) 300 K and (b) 1200K

used. This explains why Sato *et al.* [45] found that Gaussian curves fitted the data best, as there remained no traces of the main diamond peak in the spectra they deconvoluted. For the same reason Lee *et al.* [11] found the mix function more appropriate as the spectra they analyzed also had the main Raman peak present. An explanation could be that the *D* and *G* bands represent a normal statistical distribution of different bonding arrangements and therefore also a normal distribution in peak positions. The totally symmetric first order phonon peak of diamond on the other hand, represents the Lorentzian resonance of the interaction of electromagnetic radiation with the lattice vibrations in the crystal.

Table 5.1: Deconvolution results from round 1

T_A = 300 K	c-C_D peak	*D* band	*G* band	Ratio: I_D/I_G	Ratio: $I_G/I_{c\text{-}D}$
Position (cm^{-1})	1332	1427	1536		
Intensity (a.u)	9908	295	993	0.3	0.1
FWHM (cm^{-1})	2.13	168	106		
g (% Gaussian)	0.32	0.8	1		
T_A = 600 K					
Position (cm^{-1})	1332	1426	1547		
Intensity (a.u)	24 255	286	640	0.5	0.01
FWHM (cm^{-1})	2.16	148	97		
g (% Gaussian)	0.36	1	1		
T_A = 900 K					
Position (cm^{-1})	1332	1428	1571		
Intensity (a.u)	12 438	373	531	0.7	0.04
FWHM (cm^{-1})	2.19	170	92		
g (% Gaussian)	0.32	1	1		
T_A = 1 200 K					
Position (cm^{-1})	1330	1405	1595		
Intensity (a.u)	139	264	258	1	1.8
FWHM (cm^{-1})	13.9	169	79		
g (% Gaussian)	0.32	1	1		
T_A = 1 500 K					
Position (cm^{-1})	1332	-	-	-	-
Intensity (a.u)	22 616	-	-	-	-
FWHM (cm^{-1})	2.8	-	-	-	-
g (% Gaussian)	0.29				

The ratio I_D/I_G for all annealing temperatures was calculated (Table 5.1) and graphically represented in Fig. 5.5b. According to this data the amount and size of graphite-like structures increase with annealing temperature. This does not explain what happens at annealing temperature 1500K, where every indication according to the Raman data is that the diamond lattice has been completely restored. It is concluded that either the size of the graphitic regions is still below a critical value, where the restoration of the diamond structure is still possible, or the damaged structures is not purely graphitic. As seen in chapter 2 graphite is not the only carbon with Raman peaks corresponding to the *D* and *G* bands. A whole spectrum of bonding arrangements can be responsible for the peaks.

A closer look at the variation in the position of the bands with annealing temperature, as presented in Figure 5.5a, shows that the *G* band at 1536 cm^{-1} (300K) shifts to 1595cm^{-1} and the *D* band at 1426cm^{-1} (300K) to 1405 cm^{-1}, as the annealing temperature increases from 300 K to 1200 K. Various authors have shown that an upwards shift of the position of the peak at ~1540 cm^{-1} is an indication of an increasing amount of sp^3 carbon present (chapter 2.2.4). This interpretation of the data means that increasing the annealing temperature to 900K, which

shifts this peak to higher wavenumbers, increases the amount of tetrahedrally bonded carbon. The energy absorbed by the diamond lattice at these temperatures is not enough though, to complete the process. At T_A=1200K enough energy is absorbed by the atoms to cause a complete rearrangement of the structure. During this process some bonds are destroyed, others formed. And, although the spectrum resembles that of graphite, it is rather a representation of many different atomic arrangements of the carbon atoms and an intermediate phase necessary before recrystallization can occur. The drop in intensity, broadening and shift to lower wavenumbers of the main Raman band (Fig. 5.2, Table 5.1) are also indications of a complete structural change in the lattice. At annealing temperature 1500K the energy absorbed is sufficient to complete this process and restore the diamond lattice to perfect cubic symmetry.

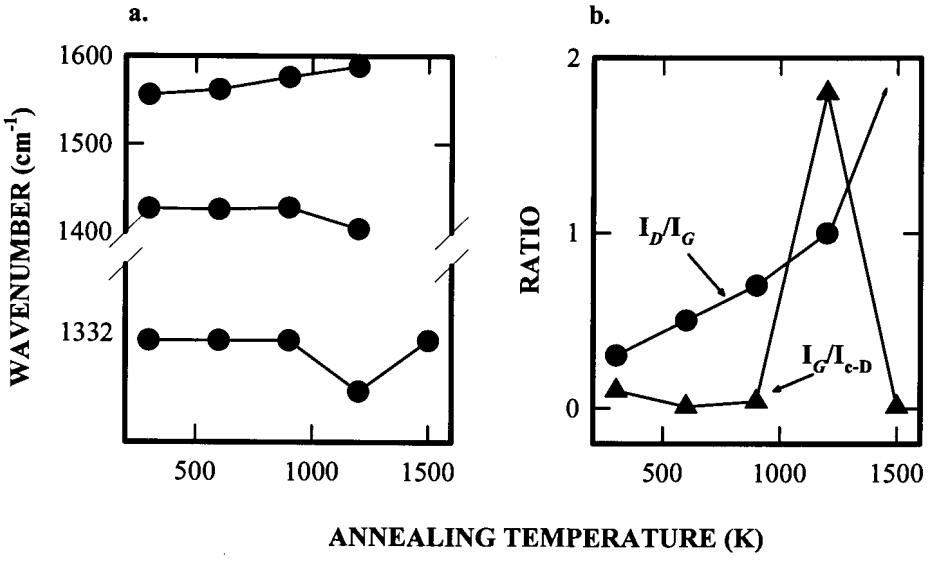

Figure 5.5: a) Variation of peak position and b) correlation of the ratios I_D/I_G and I_G/I_{c-D} with annealing temperature

The position of the diamond peak at 1332 cm^{-1} remains constant, except at 1200 K where it shifts to 1330 cm^{-1}, indicating an increase in tensile stress in the diamond lattice (chapter 2.2.1). This is in accordance with the complete atomic rearrangement described above. In Fig. 5.5b the ratio of the peak intensities of the *G* band and the peak at 1332 cm^{-1} is plotted against annealing temperature and it is clear that this graph is an approximate representation of the amount of disordered carbon in the damaged layer.

5.2.2 FTIR results:

Reflection infrared spectra of the samples were also recorded with the microscope

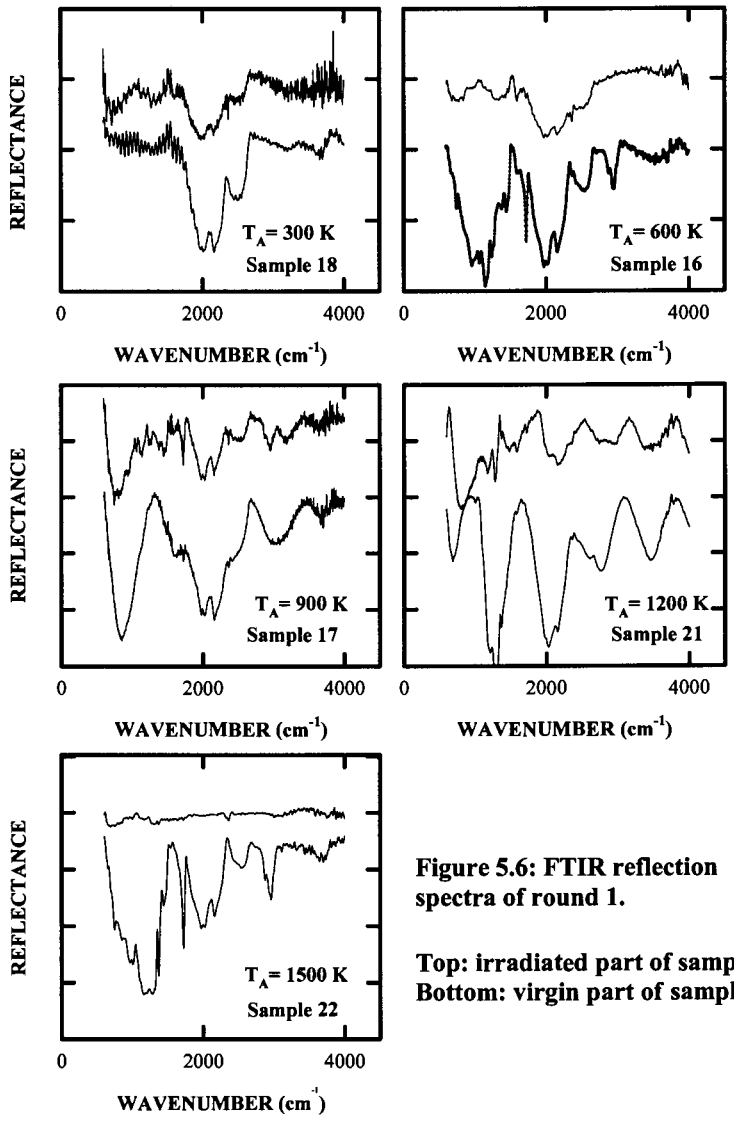

Figure 5.6: FTIR reflection spectra of round 1.

Top: irradiated part of sample
Bottom: virgin part of sample

attached to the infrared instrument. The results are shown in Fig. 5.6. Although the spectra are of a much poorer quality than the transmission spectra that were recorded of the virgin

samples (Fig. 5.1), the use of the microscope made it possible to differentiate between the irradiated part of the sample and the virgin part. For all the samples the intensity of the reflected spectrum on the irradiated part was much less than on the virgin part. Apart from the expected second order phonons spectra from some of the samples also had bands at 1700 cm^{-1} and 2900 cm^{-1}. Organic substances with carbonyl groups have bands in this region and it was concluded that the samples became contaminated with organic matter during the various analyzing processes. The presence of nitrogen bands further complicates the spectra and as the samples were not classified as the same type it is difficult to decide if differences are due to a-C_C or the presence of nitrogen.

Transmission spectra recorded of the samples in round 1 were undistinguishable from the spectra recorded of the virgin samples and the bands due to contamination were not detected. This is because the transmission spectra reflect the properties of the bulk of the sample and contamination on the surface is insufficient to produce bands that are strong enough to observe.

After having completed the experiments of round 1 the following strategy was followed for the next rounds:

- Reflection and transmission FTIR spectroscopy did not prove to be suitable methods for determining the amount of amorphous carbon present in the samples and measurements were therefore discontinued.

- Raman spectra are sensitive to the presence of amorphous carbon and will be recorded in the same way as in round 1 to enable comparisons between the rounds.

- Although interesting structural changes can be deduced from the changes in the position and shape of the bands, it was decided to use peak height ratio I_G/I_{1332} (Fig.5.5b) to compare the relative amount of disordered carbon present in the samples.

5.3 Irradiation with F = $0.3x10^{15}C/cm^2$ and F=$1x10^{15}C/cm^2$

In round 2 the same single crystal samples, after removing the damaged layer by plasma etching, were irradiated with F= $0.3x10^{15}C/cm^2$ and annealed at the same temperatures as in round 1 (chapter 4.2). In the Raman spectra recorded with the same parameters as for round 1 no bands could be detected in the amorphous carbon region for any of the samples. Analyses of the spectra conducted in the same way as in round 1 gave peak height ratios I_G/I_{1332} equal to 0 for all of the samples and, according to this, conversion to amorphous carbon was undetectable. The experimental strategy followed in round 1 could not be used and the experiment had to be redesigned.

The parameters (chapter 4.2) for recording the Raman spectra were changed to enhance the intensity of the amorphous carbon band. In contrast to the spectra of round 1, where there was only one broad peak, several small bands were observed in this region. This made it difficult to calculate the peak height ratio I_G/I_{1332} that was used in round 1. It was more useful to use the ratio, of the integrated area under all the Raman peaks in the region 1350-1700 cm^{-1} (a-C_C) to the area under the first order diamond peak at 1332cm^{-1} (c-C_D), as a relative indication of the amount of a-C_C formed. The integration program of the Dilor LabSpec® software was used to determine the area under the peaks. The results of round 1 were also analysed in the same way, compensating for the different acquisition times that were used in round 1. In round 3 the same procedures were followed and the results of the three rounds could now be compared to each other.

The results of samples irradiated with F=$0.3x10^{15}$, F=$1x10^{15}$ and F=$3x10^{15}$ C/cm^2 at different annealing temperatures are graphically presented in Fig 5.5. It shows that the amount of a-C_C formed is not linearly dependent on the fluence intensity. There is hardly any difference between the results of the samples irradiated with F=$0.3x10^{15}$ and F=$1x10^{15}C/cm^2$ and although the results from the virgin samples are not included in the figure, there was also no significant differences. Annealing at 900 K slightly increased the amount of a-C_C formed and annealing at 1200K and 1500K caused the peaks associated with a-C_C to practically disappear. In contrast to these results the increase in a-C_C formed for F=$3x10^{15}C/cm^2$ is huge and the effect of annealing at 1200K even more so (round 1). It is clear that between

irradiation levels F=1x10^{15}C/cm^2 and F=3x10^{15}C/cm^2 a critical value of F exits where the effect of implantation increases substantially and becomes visible in the Raman spectrum. It is also evident that below T_A=1200K the ratio of a-C_C to diamond does not increase significantly, but at $T_A \geq 1200$K a total structural change takes place.

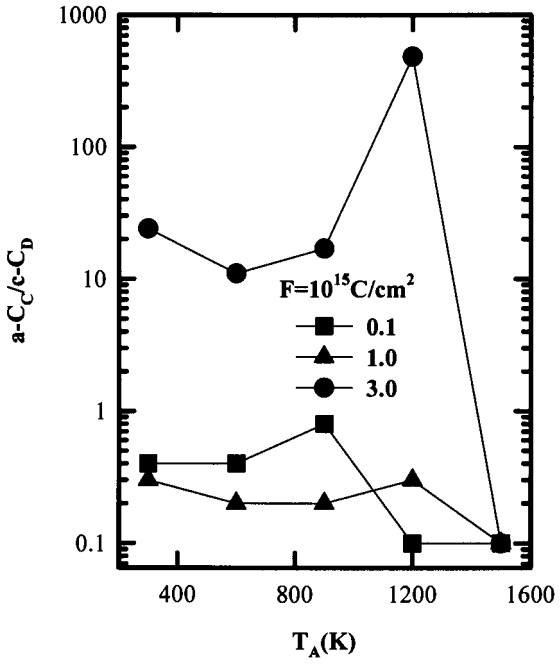

Figure 5.7: a-C_C/c-C_D at different T_A (rounds 1, 2 and 3)

In order to find a structural explanation for these observed phenomena, Raman spectra were also analyzed to determine the position and linewidth of the Raman peak at 1332 cm^{-1} and the exact position of peaks in the region 1350-1700 cm^{-1} and compared with each other. The results of rounds 1, 2 and 3 are summarized in Table 5.2.

Table 5.2: Results from rounds 1, 2 and 3

Annealing temp.	Position c-D peak	FWHM c-D peak	Bands between 1332 and 1650 cm^{-1}
Round 1: F = $3x10^{15}$ C/cm^2			
300K	1332 vs	2.6	1536 m, br
600K	1332 vs	2.6	1547 m, br
900K	1332 vs	3.1	1389 w, br; 1571 m, br
1200K	1328 w	21	1405 m, br; 1595 br
Round 2: F = $0.3x10^{15}$ C/cm^2			
300K	1332 vs	2.8	1555 vw, br
600K	1332 vs	3.1	1575 vw, br
900K	1332 vs	2.1	1441vw ,1492 vw, 1590 vw, sh; 1635 vw, br, 1810 vw
1200K	1332 vs	2.5	-
1500K	1332 vs	2.2	-
Round 3: F = $1x10^{15}$ C/cm^2			
300K	1332 vs	1.9	1555 vw, br
600K	1332 vs	1.9	1547 vw, br
900K	1332 vs	1.85	1492 vw, 1590 w, sh; 1635 w, br
1200K	1332 vs	2.1	-
1500K	1332 vs	2.4	-

vs = very strong, s = strong, m = medium, w = weak , vw = very weak, br = broad, sh = shoulder

In Fig. 5.8a the spectra recorded of the samples irradiated with F=$3x10^{15}$C/cm^2 and annealed at 300 K and 1200 K respectively are compared. The spectrum of the sample annealed at 300K displays the typical sharp and intense diamond peak associated with crystalline diamond, in addition to a broad peak around 1536 cm^{-1}, which is usually assigned to a-C_C. In the spectrum of the sample annealed at 1200K the diamond peak has broadened (from 2.5 cm^{-1} to 21 cm^{-1}) and dropped considerably in intensity, which means that the crystallinity of the diamond structure has decreased. The broad peak at 1536 cm^{-1} shifted to 1595 cm^{-1} and broadened until it overlaps with the diamond peak at 1332 cm^{-1} (round 1). This is in contrast to what happens in round 2 and round 3.

In rounds 2 and 3 (F = 0.3 x 10^{15} C/cm^2 and F = 1 x 10^{15} C/cm^2) it was impossible to detect the irradiated part on the samples visually and spectra were therefore recorded on both sides of each sample. The side with the most intense peaks present in the region was taken as the irradiated side. There was no difference in position or linewidth of the Raman peak at 1332 cm^{-1} and only very weak peaks were observed in most of the samples (Table 5.2). The most intense peaks were found in the sample irradiated with F=$1x10^{15}$/cm^2 and T_A=900K and in Fig. 5.8b the spectrum of this sample is displayed. Although very weak, distinct bands are

visible at 1441, 1493, 1590, 1635 and 1810 cm^{-1}, while only a weak peak, centered at 1540

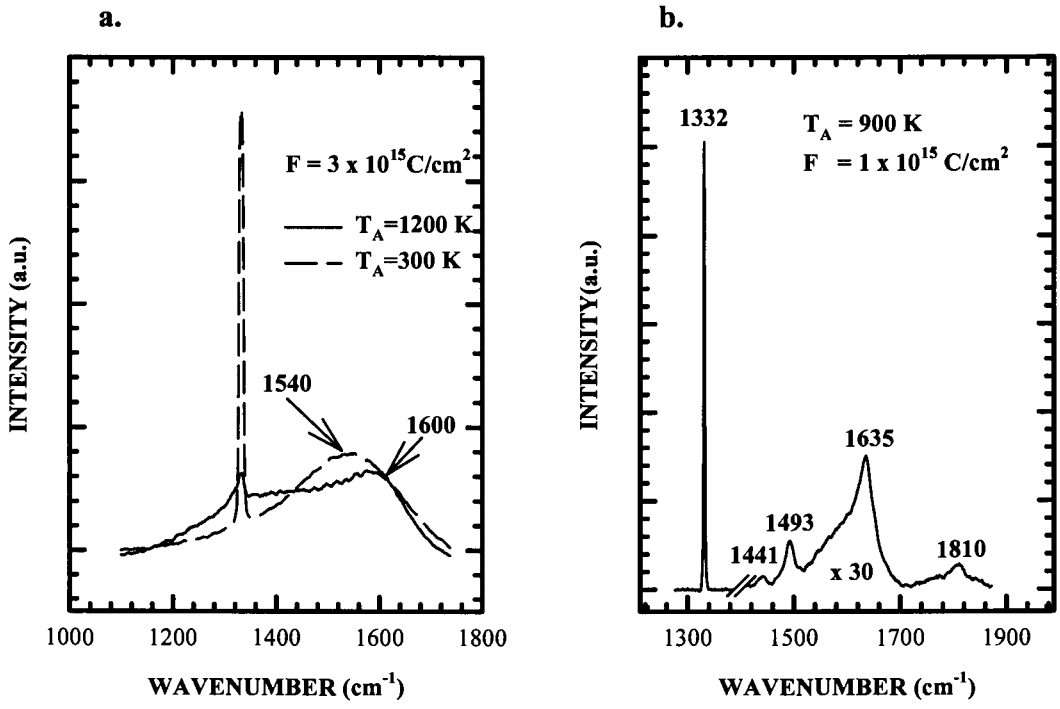

Figure 5.8: Comparison of radiation damage in samples a) F = 3x10^{15}C/cm^2 and b) F = 1x 10^{15}C/cm^2

cm^{-1}, was observed on the other side. The samples annealed at temperatures 1200K and 1500K had no bands in this region.

Similar bands have been reported (1422, 1447, 1467, 1496, 1540, 1563, 1631, 1649, 1683 and 1726 cm^{-1}) for MeV ion implantations [31]. The appearance of these bands were explained by the effect of internal pressure, exercised by the stiff overlaying diamond layer, on the formation of different bonding structures. Although low fluence implantation levels were used in these experiments, there was no volume expansion (stress release) and the underlying layers could be under the same pressure as for high fluence implantations. It should be noted that these bands are extremely weak and could only be observed by increasing the acquisition time. In this case the diamond lattice is not influenced as the position and linewidth of the diamond band at 1332 cm^{-1} stays the same. A possible explanation is that localized C-C double (sp^2) and even triple bonds (sp^1) form to accommodate the extra carbon atoms in the rigid

diamond lattice, as the bands occur on positions where these bonds display Raman bands. For $F \geq 3x10^{15} C/cm^2$ the total energy transferred into the diamond lattice is enough to expand the overlaying diamond structure (as seen with atomic force measurements [56]), making it possible for different structures to form. At high annealing temperatures a total reorganization, which involves the whole structure, takes place.

5.4 Irradiation through a metal grid

In round 4 irradiation took place through a metal grid (Fig. 4.1) to simulate "data storage" by creating "pixels" ($7.4x7.4\ \mu m^2$) separated by 5μm wide non-irradiated material. A visual inspection of the samples showed that on the heavily implanted samples the grid was clearly visible. Raman spectra could be recorded on the damaged area, as well as on the areas in between. On the two samples irradiated with $F=0.3\ x10^{15} C/cm^2$ it was very faint and on the sample irradiated with $F=0.1\ x10^{15} C/cm^2$ it could not be seen at all. For this reason Raman spectra of this sample were recorded in a straight line every 2 μm, but no significant variation in the amount of a-C_C could be detected. The Raman measurements corroborated these visual results (Table 5.3) and confirm the results from round 1.

A visual inspection of the samples after annealing (1700K, 5 min.) showed that only in the samples irradiated with $F=10x10^{15}\ C/cm^2$ and $F=3x10^{15}\ C/cm^2$ were the imprint of the grid

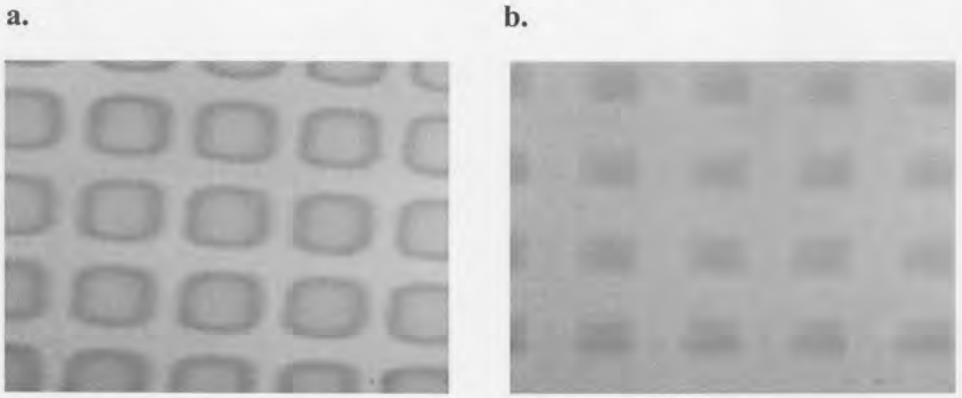

Figure 5.9: Video images of (a): sample irradiated with $F = 10x10^{15} C/cm^2$ and (b): $F = 3x10^{15} C/cm^2$ after annealing at 1700K for 5 min.

that was used still discernible. In fact, for the sample irradiated with $F=10x10^{15} C/cm^2$ the mask

imprint was even more visible than before annealing and had the exact dimensions of the mask (Fig. 5.9a). For the sample irradiated with F=3x10^{15}C/cm^2 the imprint was much weaker and the size of the darkened areas had decreased (Fig. 5.9b).

Recrystallization must have occurred on the edges of the implanted areas. This has been confirmed by the Raman results and is reconcilable with the channeling results [56]. For both of these samples significant line broadening of the diamond peak at 1332 cm^{-1} occurred (in most spectra recorded of the sample irradiated with F=1x10^{16}C/cm^2 this peak did not exist), while for the rest of the single crystal samples there were no changes in position and linewidth of this band.

Table 5.3 Raman bands from spectra at different F and T_A from rounds 4

T_A	c-D peak (cm^{-1})	FWHM of c-D peak (cm^{-1})	Peaks (cm^{-1})
F = 0.1x10^{15} C/cm^2			
300K	1332 vs	2.6	-
1700K	1332 vs	3	-
F = 0.3x10^{15} C/cm^2			
300K	1332 vs	2.8	-
1700K	1332 w	2.8	-
F = 1x10^{15} C/cm^2			
300K	1332 vs	2.45	-
1700K	1332 vs	5.5	-
F = 3x10^{15} C/cm^2			
300K	1332 s	2.1	1540 m, br
1700K	1332 m	5.5	1600 m
F = 10x10^{15} C/cm^2			
300K	1328 w	2.1	1540
1700K	1360 w, br	-	1600 w, br

vs = very strong, s = strong, m = medium, w = weak , vw = very weak, br = broad, sh = shoulder.

In Fig.5.10 a and b the spectra of the sample irradiated with F=3x10^{15}C/cm^2 and annealed at T_A=300K and T_A=1700K, are plotted to the same scale. The ratio of the a-C_C/c-C_D bands had increased from 7.5 for the sample annealed at 300K to 55 for the sample annealed at 1700K and the position of the a- C_C band had also shifted from ~1540 cm^{-1} to ~1600 cm^{-1}. Raman spectra of the F=10x10^{15}C/cm^2 implanted sample (Fig. 5.10 c and d) have changed after annealing at 1700K and display the distinct characteristics of a-C_G with the disorder

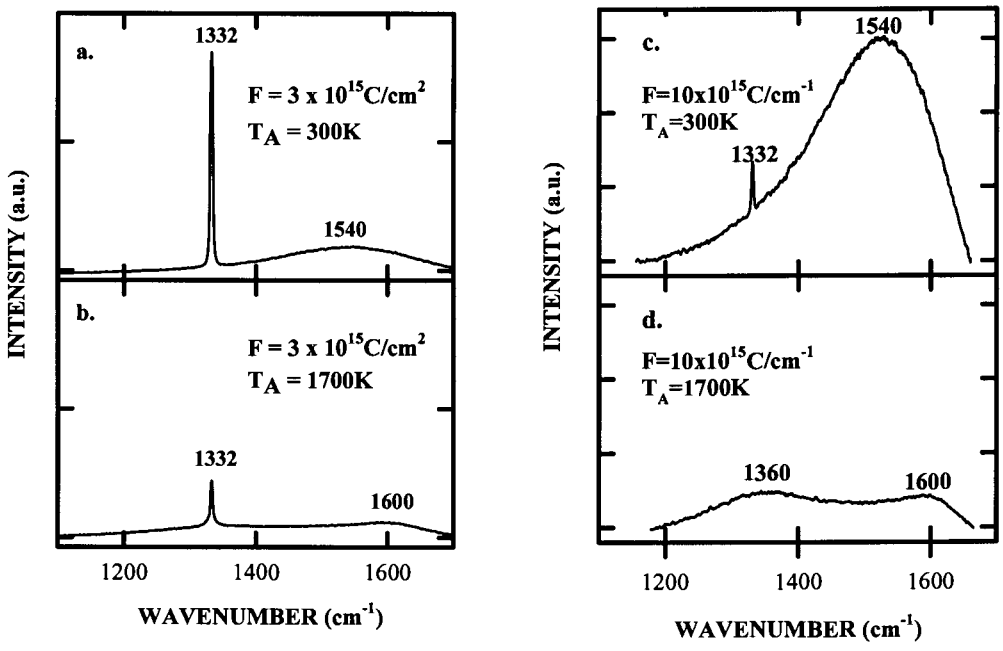

Figure 5.10: Raman spectra of samples irradiated with F=3x10^{15}C/cm^2 and F=10x10^{15}C/cm^2 at different annealing temperatures

induced D line near 1360 cm^{-1} and the G line greater than 1575 cm^{-1}. It can be seen that at T_A = 300K (Fig 5.10a) the spectrum displays only one broad band around 1540 cm^{-1}, with a weak peak at 1332 cm^{-1} (c-C_D).

5.5 Comparison of annealing conditions

In the first two rounds the samples (F=3x10^{15}C/cm^2) were annealed at different temperatures for 1h. It was found that T_A=1200K caused a complete restructuring of the diamond lattice, while at T_A=1500K the lattice has been restored to perfect crystalline perfection according to the Raman data (Fig. 5.2).

In round 4 the samples were annealed at 1700K for 5 min and in Fig, 5.10b the spectrum for the sample with F=3x10^{15}C/cm^2 is shown. It is clearly different to the results in round 1 and it should be noted that this spectrum was recorded in the middle of the damaged

areas. Spectra recorded on the edges of the areas showed that recrystallization had occurred (Fig. 5.9b) and resembled that of perfect diamond crystals.

The damage has been completely repaired after annealing at 1500K for 1h and only partially after annealing for 5 min. at 1700K. This confirms that annealing at lower temperatures for extended periods restores damage better than rapid thermal annealing [57].

5.6 Depth profile of irradiation damage

Inspecting the sample ($F=10x10^{15}C/cm^2$, $T_A=1700K$) from round 4 visually on the video camera, it was noticed that the very visible grid pattern was on a different focal level as the top surface of the sample. It was observed with all three of the objectives (x10, x50 and x100) of the microscope, the effect differing with the penetration depth of the exciting line for each objective. It was decided to compile a depth profile of the damaged layer and therefore the axial resolution of the instrument was determined.

The method, described in chapter 3.2.6 to determine the axial resolution using silicon, cannot be applied to a virgin diamond sample due to the transparency of the sample and a different method was used. An intensity curve for a virgin sample was obtained by recording spectra of the main Raman peak at 1332 cm^{-1} in steps of 1 μm along the z-axis. Data were collected moving downwards, as well as upwards along the z-axis revealing an instrumental backlash of ~2.5μm. This can be seen in Fig. 5.11, where it is clear that the maximum intensity did not occur at the same position for the two directions.

By assuming a Gaussian resolution function the standard deviation σ and the position of the surface z_o can be obtained by fitting the experimental data points of Fig. 5.11 to an error function defined by [59]:

$$F(z) = \frac{1}{2}[1 + erf(x)] \tag{5.4}$$

with $$erf(x) = \frac{2}{\sqrt{\pi}} \int_0^x \exp(-t^2)dt \tag{5.5}$$

and $$x = \frac{z - z_o}{\sqrt{2}\sigma} \tag{5.6}$$

The standard deviation σ was found to be 1.08 for forwards scanning and 1.18 for backwards scanning. The FWHM could then be calculated using the following relationship:

$$FWHM = \sqrt{8\ln 2}\sigma = 2.3548\sigma \tag{5.7}$$

The FWHM or spatial resolution was found to be 2.54 and 2.77 for the downward and upward movements respectively, resulting in a mean value of 2.655 μm.

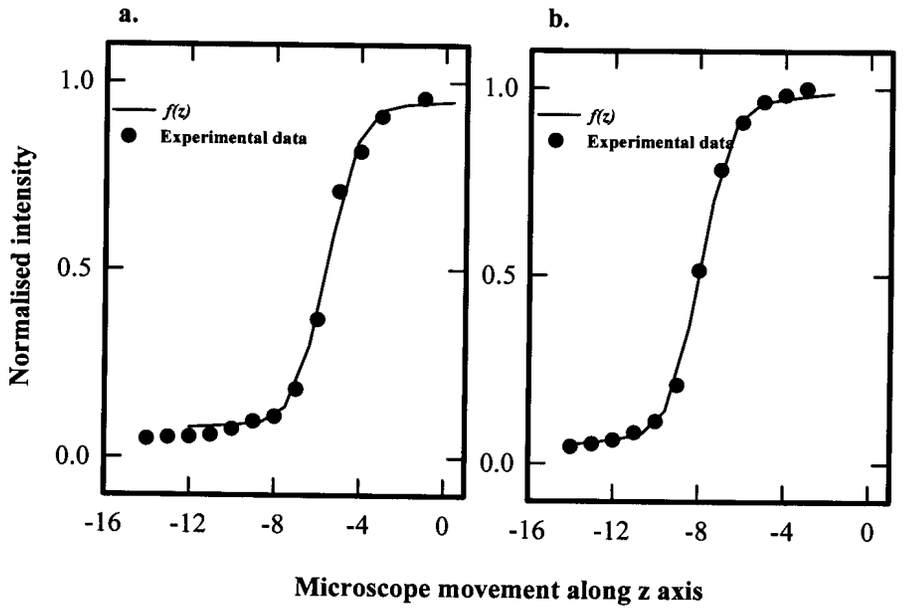

Figure 5.11: Experimental results of intensity distribution for (a): forwards scanning and (b): backwards scanning with fitted error function.

This means that for the experimental setup used during these experiments an "optical section" of Δz=2.5 μm was sampled for the recording of each spectrum. The 3-D figures obtained by adding the spectra obtained for different z values thus have an artificially extended depth of focus [53] as 2.5μm is sampled for each spectrum. This is illustrated with data collected in round 1 from sample 17 ($F=3x10^{15}/cm^2$, $T_A = 900$ K), as seen in Fig.5.12. It is

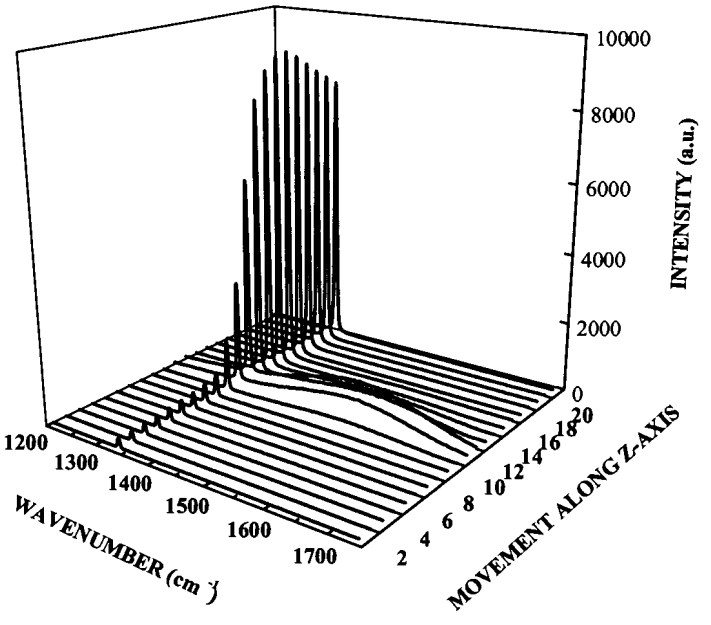

Figure 5.12: Depth profile of sample 17 (round 1), $F=3x10^{15}C/cm^2$, $T_A = 900K$, moving along z-axis in steps of 2μm.

clear that the damaged layer was observed in more than one spectrum, although the thickness of the damaged layer is less than 200nm, as determined by other techniques [56]. The intensity profile of the main diamond band follows the exact pattern as for the virgin sample and was therefore not influenced by the irradiation. The normalized intensities of the diamond peak at 1332 cm^{-1} and the broad peak caused by amorphous carbon around 1500 cm^{-1} were plotted against the movement along the z-axis of the microscope objective in Fig.5.12. The instrument resolution can be determined directly from the graph as the FWHM of the Gaussian peak formed by the intensity of the thin layer [60]. In this instance it was determined to be 2.5 μm, which confirms the values calculated from eq. 5.7.

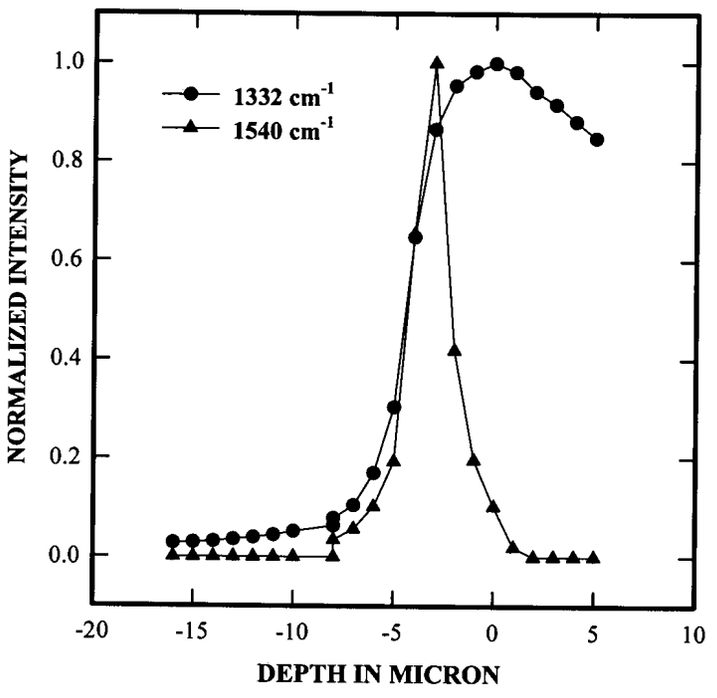

Figure 5.13: Normalized intensity depth profile of the data collected in round 1 for sample 17 ($F=3x10^{15}C/cm^2$, T_A = 900 K)

The depth profile of sample 18 in round 4 ($F=10x10^{15}C/cm^2$, T_A=1500K) was obtained by recording spectra on the same spot with the confocal microscope moving along the z-axis in steps of 4 μm. It is shown in Fig. 5.14 and is plotted to the same scale as the depth profile of sample 17 from round 1 (Fig.5.12).

It clearly shows that the damage is concentrated in a layer under the top surface of the diamond and the absence of the diamond peak in the graphite-like layer is an indication that there is no c-C_D left in this layer (this does not exclude a minor fraction of sp^3 bonded carbon) and that the signal from the undamaged diamond layer below the surface is cut out. A thin diamond layer is still visible on top of the damaged layer. This is in agreement with the optical data obtained for the same sample, which shows that the damaged layer absorbs UV light in this region [57]. Upon deeper penetration into the sample though, the diamond peak is observed (but damped). This can only be explained if the high irradiance level ($1.25x10^3$ kW/cm^2) of the focused laser beam at the sample is taken into account. This is much higher

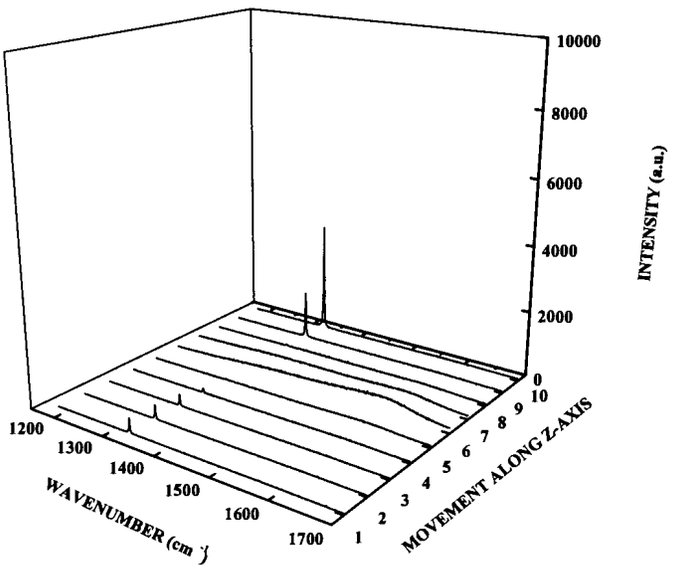

Figure 5.14: Depth profile of sample 18, ($F=10x10^{15}C/cm^2$, $T_A=1500K$) moving in steps of 4 μm along the z-axis

than that used in the optical absorbance experiments and together with the unusual intensity of the first order diamond peak and the thinness of the graphitic layer, explains why the diamond peak of the diamond layer underneath the graphitic layer can be observed.

Analysis of the spectra recorded above and below the graphitic layer revealed that the position of the first order diamond peak had shifted to 1327 cm^{-1} (tensile stress) and the FWHM has increased to 4 cm^{-1} in both cases. Rossi *et al.* reported a similar peak at grain boundaries of polycrystalline diamond [55], which they attributed to the formation of hexagonal diamond, which has a peak at this position. Clearly, even though there are no peaks visible in the amorphous carbon region the diamond lattice has been influenced by the implantation and deviates slightly from the perfect cubic structure and it could be that hexagonal diamond has formed.

5.7 The polycrystalline sample (X1)

As previously mentioned infrared and Raman measurements of the virgin polycrystalline sample showed it was highly crystalline and free of any impurities. The only

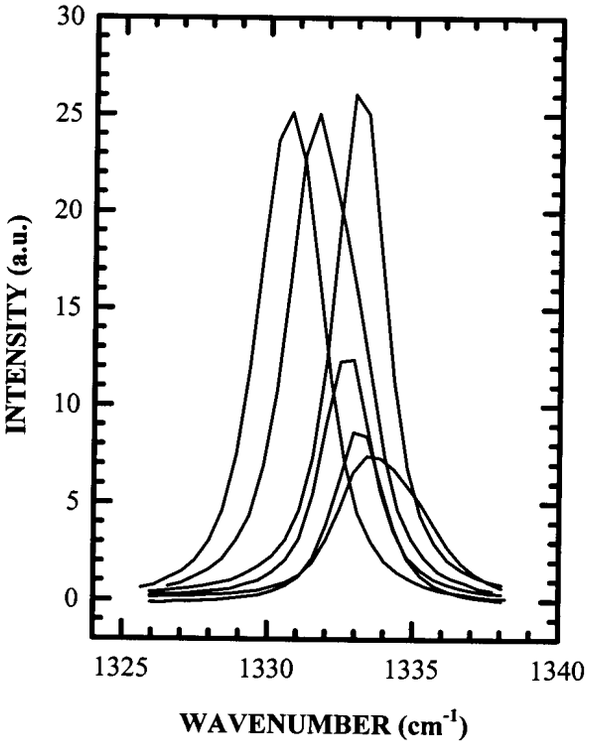

Figure 5.15: Variation in intensity, FWHM and position of c-C_D peak at different locations on the virgin polycrystalline sample.

difference from a high quality single crystal sample is the varying positions of the first order phonon (Fig. 5.15), which indicates that there are variations in internal stress in the sample. This could be an effect caused by recording spectra on grain boundaries, which can be seen in Fig. 5.16.

In round 4 this sample was irradiated with $F=1x10^{15}$ C/cm^2. Similar results were obtained as for sample 16, which were irradiated with the same fluence intensity (Fig 5.7). Annealing at 1700K caused even more variation in the position of the diamond peak and in some cases the band was even split in two. Before annealing at 1700K the mask pattern was only faintly visible and there were no bands in the amorphous carbon region. After annealing at 1700K the mask pattern could not be seen and spectra were recorded on random positions

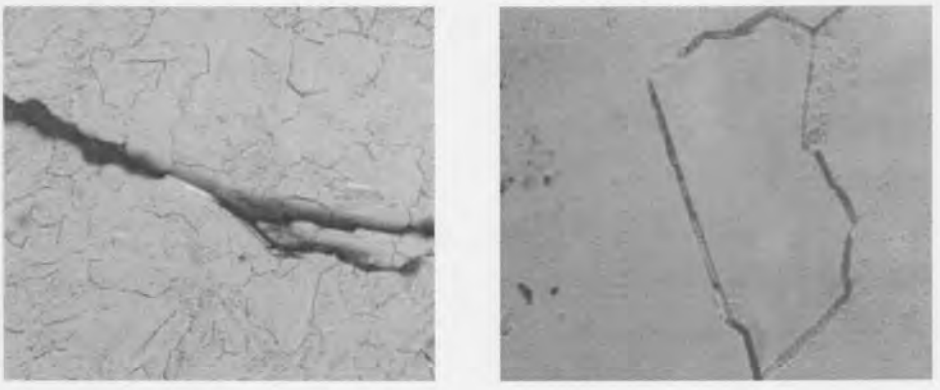

Figure 5.16: Cracks on the surface of the polycrystalline sample, after annealing at 1700K in round 4, vieved with different magnifications.

on both sides of the sample. A broad band was present at 1600 cm^{-1} on both sides, but with higher intensity on one of the sides. This band was higher in intensity than in sample 16. As the grain boundaries were more clearly visible on the video screen after annealing at 1700K, this could possibly be caused by the presence of graphite between grain boundaries.

5.8 Infrared measurements

Transmission infrared spectra were recorded of all the samples in rounds 1, 2 and 3, as well as for T_A = 300K and T_A = 1700K in round 4. Except for a slight decrease in intensity, the spectra recorded in all the rounds (after implantation, as well as after annealing) were indistinguishable from the spectra recorded for the virgin samples. This is to be expected as transmission spectra reflect the properties of the bulk of the samples and, as seen with the

Raman measurements, the changes that occurred during irradiation were small and localized to a layer just below the surface of the samples. Differences between the samples (Fig 5.1) were also greater than any change caused by irradiation.

The reflection infrared spectra (Fig. 5.6) recorded for the samples of round 1 did show large differences between irradiated and virgin parts of the samples, but interference from peaks caused by surface contamination made it difficult to interpret. As with the transmission spectra, differences between samples due to nitrogen impurities dominated the spectra.

The FTIR measurements were used to classify the virgin samples according to nitrogen impurities present (III.A).

CHAPTER 6

CONCLUSION

The Raman spectra of diamond, graphite and the various sp^2-sp^3 carbon mixtures are sufficiently distinct to make the monitoring of the modification of diamond samples by irradiation with varying fluences of ^{13}C ions possible. It was found that for $F>3x10^{15}$ C/cm^2 the damage was irreversible, for a $F=3x10^{15}$ C/cm^2 the damage was only partly repaired after annealing at 1700K and for $F<3x10^{15}$ C/cm^2 the crystalline/amorphous contrast was reversible. For $F<1x10^{15}$ C/cm^2 Raman spectroscopy was not sensitive enough to detect the incurred damage. Infrared spectroscopy was used to compare the samples with each other as to impurities present in the diamond structure.

The very interesting Raman results from round 1, where annealing for 1h at 1500K restored the diamond lattice, were partly confirmed by luminescence and atomic force measurements of the same samples. Since the other techniques used did not confirm these results it was not included in the publication culminating from this work [5]. The findings in this study suggest that a further investigation is necessary to elucidate some of the unanswered questions encountered. In this regard it would be extremely helpful to study the annealing behaviour of a sample irradiated with $F=3x10^{15}$C/cm^2 at T_A=1500K *in situ*. It would also be helpful to study the conducting properties of some of the samples, as this could give additional information about the change in electronic structure caused by implantation damage.

The basic research conducted during this study into the origin and positions of the peaks in the Raman spectra of carbon and its allotropes is currently being used in two other investigations, namely:

- The graphitization of pitches and cokes for industrial purposes conducted by Dr Morgan of the Chemical Engineering Department, two students and myself.

- The use of vitreous carbon foam in flame-retardant conducted by Dr. W Focke of the Institute of Applied Materials, Johan Labuschagne (Chemical Engineering PhD student) and I.

REFERENCES

1. Kneller H., Encyclopedia of Physics XVIII/2, ed. Flügge S., (Springer Verlag, Berlin, 1966) pp. 465-467.

2. Freytag W., in: Computing in High Energy Physics, eds. L. O. Hertzberger and W. Hoogland (Elsevier Science Publ., North Holland, 1986) pp. 123-134.

3. Ecker R., in: Technische Aspekte der Langzeitarchivierung von Daten, 4. Europärisches Bielefeld Kolloquim, 1998.

4. Kalbitzer S., VDI Berichte 666, 71 (1987).

5. Prinsloo L. C., Applied Physics A, **72**, 658-663 (2001).

6. Knight D. S. and White W. B. J., Mater. Res. **4,** 385-393 (1989).

7. Huong P. V., J of Mol. Struc., **292**, 81-88 (1993).

8. Spear, K. E., J. Am. Ceram. Soc., **72**(2), 171-191 (1989).

9. Grill A., Patel V. and Meyerson B. S., J. Electrochem. Soc., **138**(8), 2362-2367 (1991).

10. Silva S. R. P., Amaratunga G. A. J. and Constantinou C. P., J. Appl. Phys., **72**(3), 1149-1153 (1992).

11. Lee E. H., Hembree D. M. Jr., Rao G. R. and Mansur L. K., Phys. Rev. B, **48**(21), 15540-15551 (1993).

12. Elman B. S., Dresselhaus M. S., Dresselhaus G., Maby E. W. and Mazurek H., Phys. Rev. B, **24**(2), 1027-1034 (1981).

13. Palmetshofer L. and Kastner J., Nucl. Instr. and Meth. in Phys. Res. **B96**, 343-346 (1995).

14. Dillon R. O., Woolam J. A. and Katkanant V., Phys. Rev. B, **29**(6), 3482-3489 (1984).

15. Fadini A. and Schnepel F.M., *Vibrational Spectroscopy: Methods and Applications*, John Wiley & Sons, Inc. London, 1989.

16. Schrader B., *Infrared and Raman Spectroscopy*, John Wiley & Sons Ltd, London, 1995.

17. Fateley W. G., Dollish F. R., McDewitt N. T. and Bentley F. F., *Infrared and Raman Selection Rules for Molecular and Lattice Vibrations: The Correlation Method,* John Wiley & Sons, Inc. New York, 1972.

18. Ferraro J. R. and Ziomek J. S., *Introductory Group Theory and its Application to Molecular Structure,* Plenum Press, New York, 1969.

19. Rousseau D. L., Bauman R. P. and Porto S. P. S., J. of Raman Spectrosc., **10**, 253-290 (1981).

20. Adams D. M. and Newton D. C., *Tables for Factor Group and Point Group Analysis,* Beckman-RIIC Ltd, Croyden, England.

21. Nissum M., Shabanova E. and Nielson O. F., J. Chem. Ed., **77**, 633-637 (2000).

22. Brink J., Physics Applications: Optics, Course Notes 1998.

23. Klingshirn C. F., *Semiconductor Optics*, Springer-Verlag Berlin Heidelberg, 1995.

24. Cheetham A. K. and Day P., *Solid State Chemistry: Techniques*, Oxford University Press, Oxford, 1987.

25. Pierson H. O., *Handbook of Carbon, Graphite, Diamond and Fullerenes,* Noyes Publications, New Jersey, USA, 1993.

26. Sharma S. K, Mao H. K, Bell P. M.. and Xu J., J. Raman Spectrosc., **16**, 350-354 (1985).

27. Ramanan R. R., Niranjana S, Goswami N. and Lal K., Acta. Cryst., A**54**, 163-171, (1998).

28. Tuinstra F. and Koenig J. L., J. of Chem. Phys., **35**(6), 1126-1129, (1970).

29. Dresselhaus M. S., Dresselhaus G., and Eklund P.C., J. Mater. Res. **8**, 2054-2096, (1993).

30. Pimenta M. A., Marucci A., Empedocles S. A., Bawendi M. G., Hanlon N. B., Rao A. M., Eklund P. C., Smalley R. E., Dresselhaus G. and Dresselhaus M. S., Phys. Rev. B, **58(24)**, R16016-R16019 (1998).

31. Prawer S., Nugent D. N. and Jamieson D. N., Diam. Rel. Mat., **7**, 106-110 (1998).

32. Cottinet D., Couderc P., Saint Romain J. L. and Dhamelincourt P., Carbon, **26** (3), 339-344 (1998).

33. Matthews M. J., Pimenta M. A., Dresselhaus G., Dresselhaus M. S. and Endo M., Phys. Rev. B, **59 (10)**, R6585-R6588 (1999).

34. Mckenzie D. R., Rep. Prog. Phys., **59**, 1611-1664 (1996).

35. Shroder R. E., Nemanich R. J. and Glass J. T., Phys. Rev. B, **41**(6), 3738-3745 (1990).

36. Sinha K., Menendez J., Sankey O. F., Johnson D. A., Varhoe W. J., Kidder J. N., Patel P. W. and Lanford W., Appl. Phys. Lett., **60**, 562-564 (1992).

37. Beeman D., Silverman J., Lynds R. and Anderson M. R., Phys. Rev. B, **30 (2)**, 870-875 (1984).

38. Townsend S. J., Lenosky T. J., Muller D. A., Nichols C. S. and Elser V., Phys. Rev. Lett., **69 (6),** 921-924 (1992).

39. Durig J. R., Litle T. S., Bist H. D., Rengen A. and Narayan J., J. Raman Spectrosc., **23**, 625-628 (1992).

40. Gilkes K. W. R., Prawer S., Nugent K. W., Robertson J., Sands H. S., Lifshitz Y. and Shi X., J. Appl. Phys., **87 (10)**, 7283-7289 (2000).

41. Zhang W., Zhang F., Wu Q. and Chen G., Mat. Lett., **15**, 292-297 (1992).

42. McNamara K. M., Williams B .E., Gleason K. K. and Scruggs B. E., J. Appl. Phys., **76 (4),** 2465-2472 (1994).

43. Namba Y., Heidarpour E. and Nakayama M., J. Appl. Phys., **72** (5), 1748-1751 (1992).

44. Bhatia K. L., Fabian S., Kalbitzer S., Klatt Ch., Krätschmer W., Stoll R. and Sellschop J. F. P., Thin Solid Films, **324**, 11-18 (1998).

45. Sato S., Watanabe H., Takahashi K., Abe Y. and Iwaki M., Nucl. Instr. and Meth., **B59/60**, 1391-1394 (1991).

46. Gronholz Jand Herres W., *Understanding FT-IR Data Processing* Dr. Alfrsd Huethig Publishers.

47. Willis H. A., van der Maas J. H. and Miller R. G. J., *Methods in Vibrational Spectroscopy*, 3rd edition, John Wiley & Sons Ltd, 1987.

48. Opus/IR Reference Manual, Bruker, 1995.

49. Bertie J. E., Pure and Appl. Chem., **70**(10), 2039-2045 (1998).

50. Pedrotti F. L. and Pedrotti L. S, *Introduction to Optics*, Prentice-Hall International, Inc, New York, U.S.A., 1993.

51. Coherent, Innova, User Manual.

52. Kelly J. J., *Electrons in Solids: Theory and Applications*, Debye Institute: Course Notes.

53. Dilor XY User Manual, 1997.

54. Morell G., Quiñones O., Díaz. Y., Vargas I. M., Weiner B. R. and Katiyar R. S., Diamond and Related Materials, **7**, 1029-1032 (1998).

55. Rossi M. C., Salvatore S. and Galluzzi F., Phys. Stat. Sol. A, **172**, 97 (1999).

56. Friedland E., Hauser T., Klatt Ch. and Demanet C. M., Applied Physics A, **72**, 664-668 (2001).

57. Dresselhaus M. S. and Kalish R., *Ion Implantation in Diamond, Graphite and Related Materials,* Springer-Verlag, Heidelberg, 1992.

58. Brink D. J., Applied Physics A, **72**, 648-652 (2001).

59. Abramowitz M. and Stegun I. A., *Handbook of Mathematical Functions,* Dover Publications Inc., New York, 1965.

60. Horiba Group, Raman Spectroscopy Application Note, T.N., **1**, 3-6 (2000).